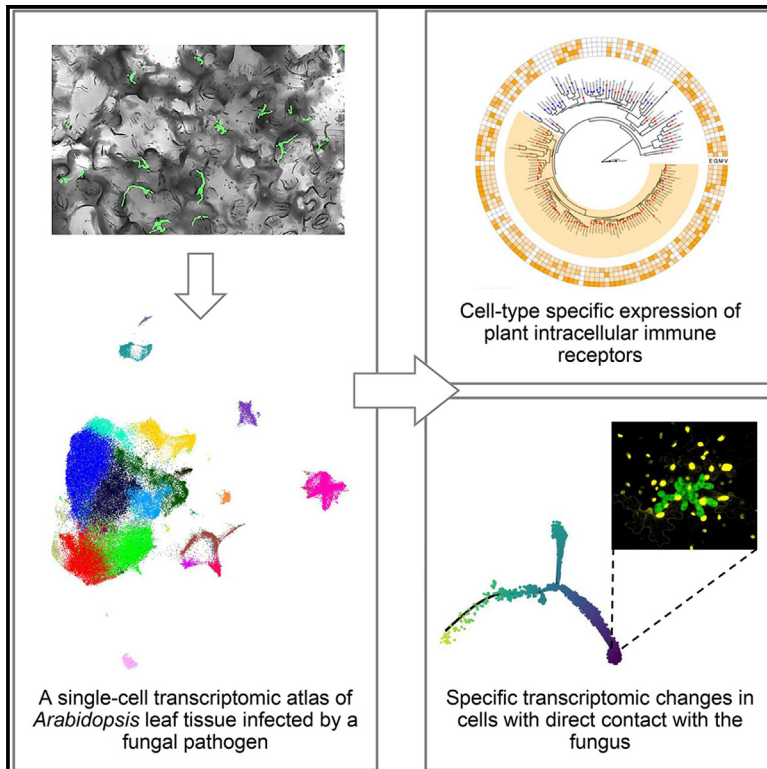


Cell Host & Microbe

Cell-type-specific responses to fungal infection in plants revealed by single-cell transcriptomics

Graphical abstract



Authors

Bozeng Tang, Li Feng,
Michelle T. Hulin, Pingtao Ding,
Wenbo Ma

Correspondence

wenbo.ma@tsl.ac.uk

In brief

Tang et al. employ single-cell transcriptomics to investigate heterogeneous responses to fungal infection. They reveal vasculature-enriched expression of specific immune receptors and define cellular processes induced by direct contact with the pathogen. This work provides a valuable resource and offers insights for studying intricate dynamics in plant-microbe interactions.

Highlights

- Single-cell RNA-seq reveals heterogeneity in plant response to fungal infection
- An *Arabidopsis* leaf atlas is generated using 95,040 single-cell transcriptomes
- Intracellular immune receptor NLRs exhibit cell-type-specific expression patterns
- Trajectory inference defines spatially dynamic responses to the invading fungus

Resource

Cell-type-specific responses to fungal infection in plants revealed by single-cell transcriptomics

Bozeng Tang,¹ Li Feng,¹ Michelle T. Hulin,¹ Pingtao Ding,² and Wenbo Ma^{1,3,*}

¹The Sainsbury Laboratory, Norwich Research Park, University of East Anglia, NR4 7UH Norwich, UK

²Institute of Biology Leiden, Leiden University, Sylviusweg 72, 2333 BE Leiden, the Netherlands

³Lead contact

*Correspondence: wenbo.ma@tsl.ac.uk

<https://doi.org/10.1016/j.chom.2023.08.019>

SUMMARY

Pathogen infection is a dynamic process. Here, we employ single-cell transcriptomics to investigate plant response heterogeneity. By generating an *Arabidopsis thaliana* leaf atlas encompassing 95,040 cells during infection by a fungal pathogen, *Colletotrichum higginsianum*, we unveil cell-type-specific gene expression, notably an enrichment of intracellular immune receptors in vasculature cells. Trajectory inference identifies cells that had different interactions with the invading fungus. This analysis divulges transcriptional reprogramming of abscisic acid signaling specifically occurring in guard cells, which is consistent with a stomatal closure dependent on direct contact with the fungus. Furthermore, we investigate the transcriptional plasticity of genes involved in glucosinolate biosynthesis in cells at the fungal infection sites, emphasizing the contribution of the epidermis-expressed MYB122 to disease resistance. This work underscores spatially dynamic, cell-type-specific plant responses to a fungal pathogen and provides a valuable resource that supports in-depth investigations of plant-pathogen interactions.

INTRODUCTION

Plant diseases pose major threats to global food security and sustainability. To devise effective resistance strategies, a comprehensive understanding of the molecular mechanisms underlying disease development is crucial. However, given the dynamic nature of pathogen infection within a host, the precise responses of different plant cells and tissues to infections remain elusive.¹ For instance, bacteria dwelling in the plant phyllosphere have been found to aggregate at preferred locations, including the base of glandular trichomes, cell junctions, and vein areas.² Frequently, these foliar pathogens gain access to the leaf apoplast through stomatal openings.^{3,4} Once inside the leaf tissue, the bacteria establish microcolonies close to certain host cells⁵ and trigger distinct cellular responses, compared with those not directly targeted by the pathogen.⁶

The non-uniform interactions between different plant cells and the invading pathogens become more prominent during the infection of fungi and oomycetes, in which the pathogens undergo a sophisticated morphological changes.^{7–11} This heterogeneity in host responses is influenced by both the distribution of the pathogen in the host tissue and its developmental changes. In a typical hemibiotrophic infection by a fungal pathogen, the process begins with spore germination on the surface of a plant tissue, leading to the formation of an appressorium. This specialized structure facilitates fungal penetration into host epidermal cells through the plant cuticle.⁹ After penetration, the fungus develops invasive hyphae (IH) and establishes bio-

trophic growth inside the infected cell.^{7,12,13} During the biotrophic infection stage, the fungal hyphae are confined within the invaded cell, which remains alive and provides nutrients to the pathogen.^{13–16} At a later infection stage, the pathogen switches to a necrotrophic growth and feeds on the dead tissue. At this time, fungal IH move from the initially infected cells into adjacent cells, which again support the biotrophic growth of the fungus.^{17,18} Finally, the infection cycle concludes with the production and dissemination of fungal spores. Relative location with the pathogen, combined with infection stage and pathogen development, shapes the specific responses as gene expression changes in individual plant cells. This underlines the importance of accounting for spatial variability in studies of plant-pathogen interactions. Furthermore, plant immune responses may also exhibit cell-type-specific features, adding to the intricacy of this highly dynamic process.

Plants have developed a sophisticated and, in most cases, robust immune system. The central components of plant immunity are immune receptors, which sense potential pathogens in the surrounding environment and activate immune signaling.^{19,20} Cell-surface-localized receptor-like kinases (RLKs) or receptor-like proteins (RLPs) recognize extracellular non-self molecular signatures.²¹ Their activation initiates downstream molecular events, including reactive oxygen species (ROS) burst, Ca²⁺ influx, mitogen-activated protein kinase (MAPK) activation, and transcriptional reprogramming.^{19,22,23} Another class of immune receptors are intracellular nucleotide-binding domain leucine-rich repeat-containing receptors (NLRs), which detect

cytoplasmic effectors delivered by pathogens into plant cells and activate effector-triggered immunity (ETI).^{19,24} NLRs in *Arabidopsis thaliana* (*Arabidopsis* hereafter) can be further classified based on their distinctive N-terminal domains as coiled-coil-NLR (CC-NLR or CNL); Toll/interleukin-1 receptor/resistance protein-NLR (TIR-NLR or TNL); and RPW8-like helper NLR (RNL), which contains the CC_R domain.^{25,26} How the expression and function of RLKs/RLPs and NLRs vary in different cell types during the dynamic pathogen infection process has not been explored.

To investigate the transcriptional heterogeneity in plant responses during pathogen infection, we employed the droplet-based single-cell RNA sequencing (scRNA-seq), which enables parallel transcriptome profiling of individual cells from a single reaction.²⁷ RNA-seq has been extensively applied to understand plant-microbe interactions,^{28–30} through which many key molecular events were identified. However, bulk RNA-seq cannot capture differences between cell populations that have distinct interactions with the invading pathogen. Other methods, such as laser-microdissection^{31,32} and fluorescence-activated cell sorting-based enrichment,³³ provide spatial information but can be labor intensive and hence have not been broadly utilized in plant pathology studies. scRNA-seq offers a unique opportunity to understand the heterogeneity in gene expression changes among different cell populations with a high resolution. In the past few years, a toolkit has been developed that enables comprehensive analyses of scRNA-seq data, further enhancing the dissection of how biological processes progress.³⁴

In this study, we determined cell-type-specific responses in *Arabidopsis* during infection by a hemibiotrophic pathogen *Colletotrichum higginsianum*. We analyzed the transcriptome of 95,040 *Arabidopsis* leaf cells at single-cell level to understand gene expression changes during biotrophic interaction with this fungal pathogen. Our dataset spanned all major cell types, enabling the discovery of extensive heterogeneity in the expression of immune receptor genes across distinct cell types. Subsequently, by combining quantitative live-cell imaging with trajectory inference analysis, we elucidated the spatiotemporal dynamics of plant responses and identified cell-type-specific processes in plant cells that had direct interactions with the fungal IH. This work demonstrates how previously unknown molecular events of plant-pathogen interactions can be uncovered using single-cell-based analyses. The scRNA-seq dataset generated from this study will be a valuable resource for exploring gene expression patterns in specific cell population(s) and for supporting in-depth investigations of the molecular mechanisms that govern disease development. This knowledge will be instrumental for the development of resistant crops that precisely express defense-related genes at the pathogen infection sites, which may minimize growth penalties of the plants.

RESULTS

Construction of an *Arabidopsis* leaf cell transcriptome atlas during *C. higginsianum* infection

We inoculated 14-day-old *Arabidopsis* seedlings with conidial suspensions of *C. higginsianum* and monitored the infection progression via live-cell imaging. We observed an extensive uneven distribution of the fungus in the inoculated tissue, and only a subset of plant cells had direct contacts with the fungus at various

developmental stages (Video S1). Based on the microscopy analysis, two time points, 24 and 40 h post inoculation (hpi), were selected for tissue collection as they represented early and late stages of biotrophic infection, respectively (Figure 1A). Protoplasts isolated from inoculated or mock-treated leaf tissues, in duplicates, were subjected to single-cell partitioning and RNA-seq using the 10× Genomics workflow. After applying quality control measures and minimizing batch effects, our dataset encompassed 95,040 cells (Figure S1A). Aligning the sequencing reads to the *Arabidopsis* genome revealed an overall coverage of 23,809 genes, representing 86.8% of all protein-coding genes in *Arabidopsis* (Table S1A). Each cell, on average, detected 2,583 genes and 5,491 unique molecular identifiers (UMIs), which are individual tags attached to every molecule of complementary DNA (cDNA) to track their original source and avoid PCR duplicates (Figure 1B).

Using the scRNA-seq dataset and a graph-based unsupervised clustering analysis, we then generated a transcriptome atlas, which contains 25 cell clusters (Figure 1C). The cell numbers vary from 20,500 (cluster 1) to 31 (cluster 25) (Table S2B). By comparing cluster-enriched genes (Figure S1B; Tables S2C and S2D) with previously established marker genes^{35–38} (Figure S1C), we assigned a specific cell-type identity to each cluster with the exception of clusters 6 and 18 (Figures 1C and S1D). 12 clusters, including the top four with the largest number of cells, were assigned as mesophyll cells, representing approximately 70% of the total cells. They are followed by vasculature (6 clusters, 13% of the total cells), epidermis (4 clusters, 8% of the total cells), and guard cells (2 clusters, 3% of the total cells).

We further analyzed the proportions of cells from different treatments in each cluster. Although samples at 24 and 40 h after mock (water) treatment were collected and analyzed by scRNA-seq separately, they share highly similar gene expression patterns, as indicated by a Pearson correlation analysis ($R^2 > 0.91$). Therefore, these two datasets were merged (named “mock”) in all the subsequent analyses. We found that the proportions of cells from different treatments varied drastically across clusters. For example, clusters 6, 13, 18, 23, and 25 consisted mostly of cells from the 40-hpi sample (Figure 1D), whereas clusters 14, 21, and 24 were primarily composed of cells from the mock-treated samples. Intriguingly, clusters 6 and 18 could not be assigned a clear cell-type identity, possibly reflecting global transcriptome reprogramming due to fungal infection. Consistent with these results, landscapes of transcriptome atlases made by cell populations from different treatments exhibited alterations in distinct cell clusters, with the most significant differences observed at 40 hpi (Figure 1D).

To account for potential skewing of the analysis by the protoplasting process during sample preparation, we evaluated gene expression changes caused by protoplast isolation, using bulk RNA-seq (Table S1E). We found that protoplasting-induced transcripts were generally below 5% in each cluster, and this proportion was relatively constant across the clusters, suggesting that these expression changes did not result in a shift of cell populations (Figure S1E). We also assessed potential cell damage during protoplasting by monitoring sequencing reads derived from mitochondrial and chloroplast genes. In general, only about 1% of total reads were from mitochondrial and chloroplast genes

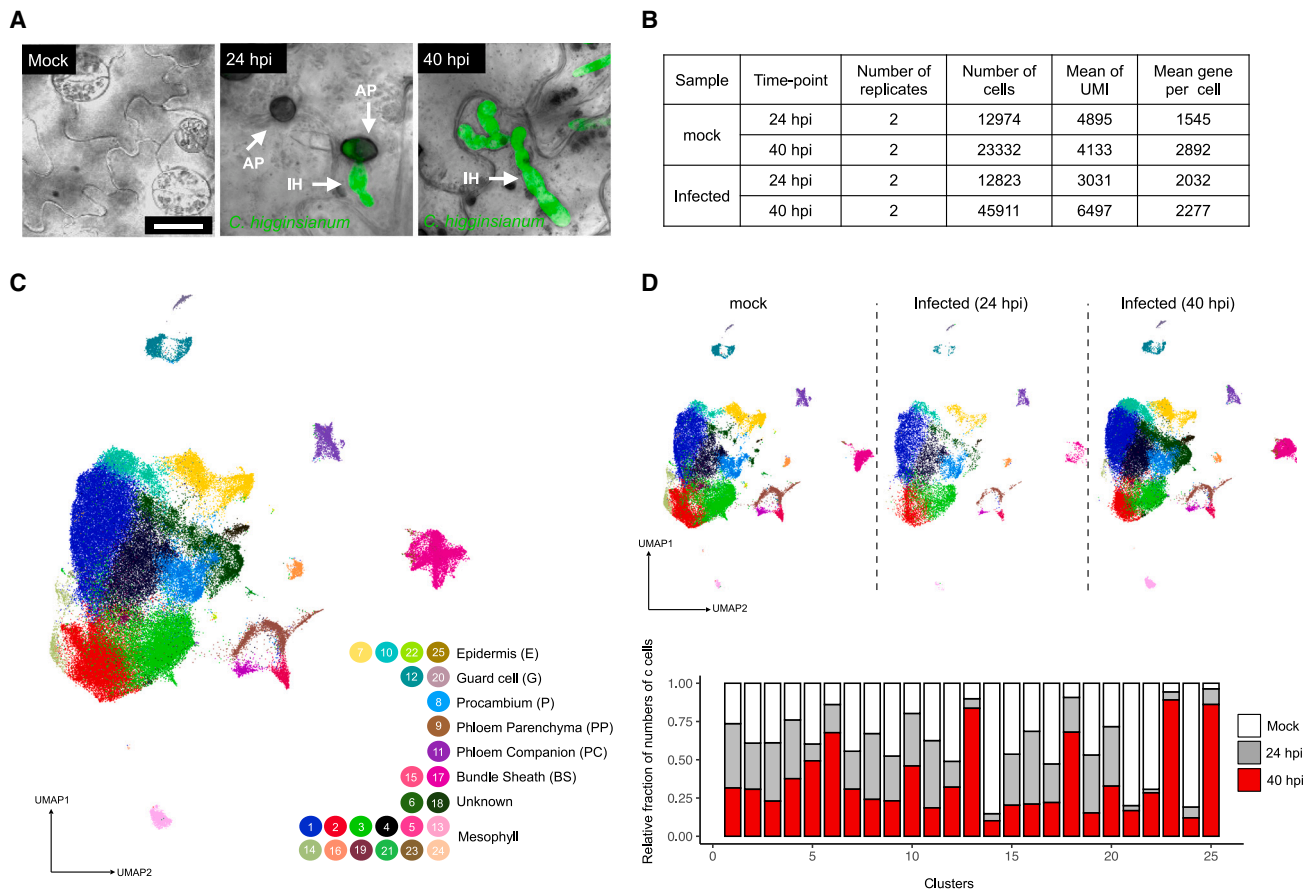


Figure 1. Construction of an *Arabidopsis* leaf cell transcriptome atlas during fungal infection

(A) Micrographs of *Arabidopsis* seedlings inoculated with conidial suspensions of *Colletotrichum higginsianum*. A transgenic fungus constitutively expressing green fluorescence protein (GFP) was used to facilitate visualization. Images were taken at 24 and 40 h post inoculation (hpi). Appressoria (AP) and invasive hyphae (IH) are indicated with arrowheads. Mock, water treatment. Scale bars, 10 μ m.

(B) A summary of processed scRNA-seq data using *Arabidopsis* leaf tissues at 24 and 40 h after mock treatment or fungal inoculation. Unique molecular identifier (UMI), transcripts detected per cell.

(C) A transcriptome atlas consisting of 95,040 cells. Each cell is represented by a dot on a plot visualized by uniform manifold approximation and projection (UMAP). Based on transcriptional signatures, the cells were divided into 25 clusters using graph-based, unsupervised clustering. Each cluster was assigned to a cell type except for clusters 6 and 18.

(D) Transcriptome changes in response to fungal infection captured by scRNA-seq. Upper panel: separate single-cell atlas generated from mock-treated and infected tissues. The 25 clusters described in (C) are presented in each atlas. Lower panel: proportions of cells from mock, 24-hpi, or 40-hpi samples in each cluster. The proportions were normalized against the total number of cells in each sample.

in each cell. Similar to the protoplasting-induced genes, the relative abundance of these transcripts was also constant across all the clusters (Figure S1F). These results indicate that the specific transcriptome signatures and the clustering of cell populations were primarily determined by cell type and responses to fungal infection. Collectively, we generated a single-cell transcriptome atlas that covered all major cell types in *Arabidopsis* leaf tissues and captured dynamic gene expression changes during biotrophic infection by a fungal pathogen.

Cell-type-specific expression of genes encoding immune receptors

Using the transcriptome atlases created from both the mock-treated and infected samples, we identified 1,937 differentially expressed genes (DEGs) that showed upregulation or downregulation in certain cell type(s) during fungal infection

(Table S2A). Notably, some of these genes were considered as exhibiting unchanged expression when we reanalyzed the data from a previous bulk RNA-seq using the same *Arabidopsis*-*C. higginsianum* pathosystem.⁷ Nonetheless, our study revealed differential expression of these genes in a cell-type-specific manner (Figure 2A). We also noticed that some DEGs identified from the bulk RNA-seq were not detected in our single-cell-based analysis (Figure S2A). These results suggest the importance of conducting transcriptomic analysis at both single-cell and whole-tissue levels.

Given the crucial role of intracellular immune receptors, NLRs, in plant defense, we investigated their expression patterns across different cell types. From the genome of *Arabidopsis* ecotype Col-0 and using NLRtracker,²⁵ we identified 214 genes encoding putative NLRs, among which 169 were detectable in our scRNA-seq dataset (Table S2B). To mitigate potential bias

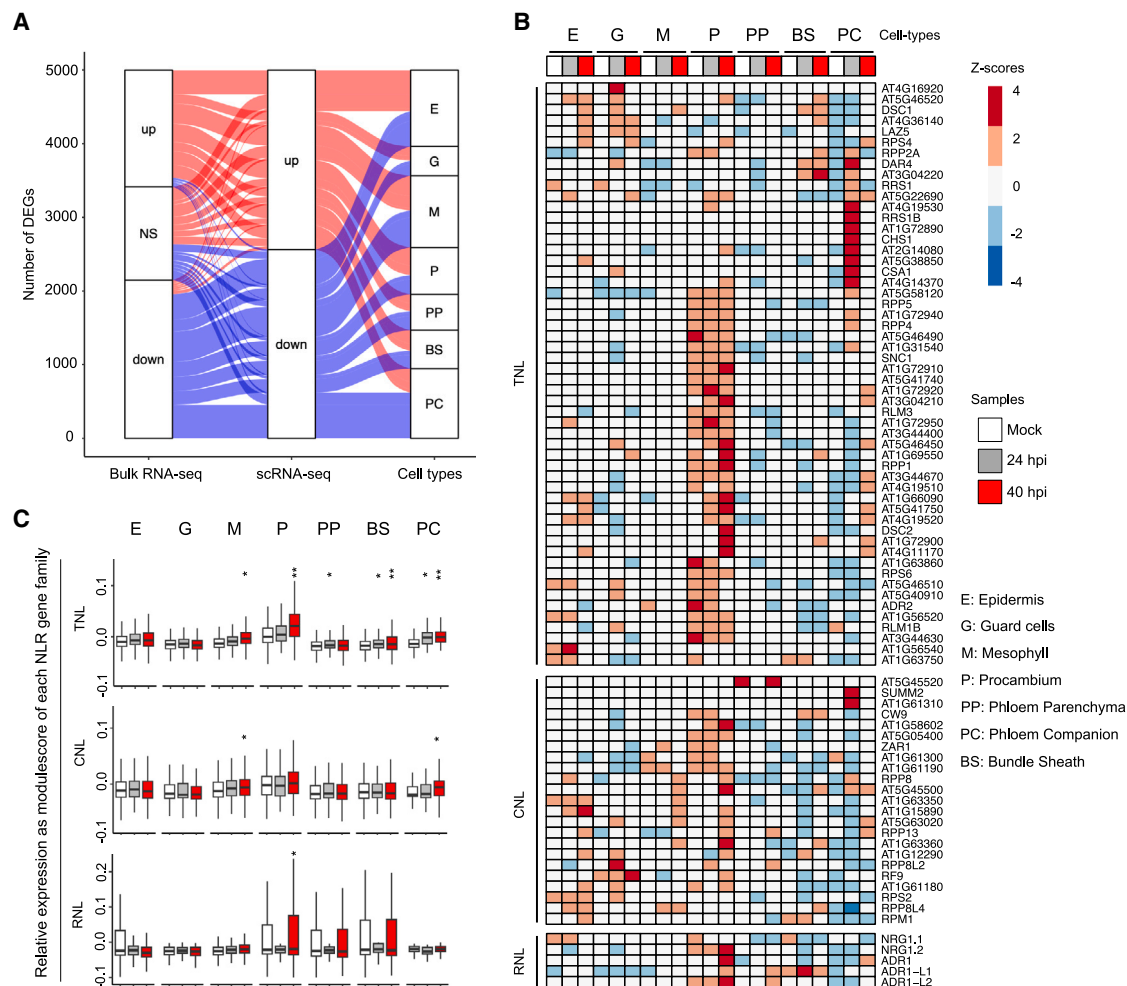


Figure 2. Cell-type-specific expression of intracellular immune receptors in *Arabidopsis*

(A) Many differentially expressed genes (DEGs) identified in scRNA-seq are masked in bulk RNA-seq. DEGs detected from a published bulk RNA-seq dataset (ENA projects accessions: PRJNA148307). “NS”: genes that were not considered as DEGs in bulk RNA-seq but showed differential expression in a cell-type-specific manner based on scRNA-seq. DEGs calling from the scRNA-seq data was done by FindMarker with default settings in each annotated cell type. DEGs calling from the bulk RNA-seq used cutoffs of $\log_2|FC| > 2$ and $p \text{ adj} < 0.05$.

(B) Cell-type-specific expression and induction of NLRs by fungal infection. Heatmaps show relative expression of known or predicted NLR-encoding genes from *Arabidopsis* Col-0 in each annotated cell type and with or without fungal infection. Gene expression levels are represented by aggregated UMI counts in all the cells belonging to the same cell type and in the same treatment.

(C) Significant induction of TNLs in vasculature cells after fungal infection. Boxplots show normalized expression of all genes belonging to the same NLR family from each cell type. Relative expression of an NLR was normalized to 50 randomly selected genes in the same cell. The normalized expression levels of genes belonging to the same NLR family in the same cell type were then aggregated and compared between mock-treated and fungal infected samples. t test was used to determine significant differences. * $p < 0.05$ and ** $p < 0.01$.

caused by low expression of some of these genes (Figure S2B), we focused on genes with more than 500 normalized read counts for further analysis (Table S2C). Employing these criteria, 98 genes were analyzed by determining their relative expression levels in each cell type in both mock-treated and infected samples. Interestingly, a significant portion of TNL genes, including those encoding known TNLs such as RPP1, RPP5, SNC1, and RPS6, were predominantly expressed in procambium cells (Figure 2B). Many of these procambium-expressed NLR genes were further induced after fungal infection. Procambium cells serve as the source of primary phloem and xylem cells.^{39,40} Notably, another subset of TNL genes are highly, and almost exclusively,

induced in phloem companion cells at 24 hpi but not at 40 hpi (Figure 2B). These include genes encoding known TNLs such as RRS1B, CSA1, and CHS1. This pattern of transient induction may be a consequence of a potential pathogen suppression of host immunity. A small number of TNLs were induced by fungal infection in multiple cell types. For example, RPS4 showed increased expression in epidermal, guard, procambium, and phloem companion cells.

RNLs play an essential role in immune signaling, especially immune activation by TNLs. Consistent with the vasculature-enriched expression of TNLs, we also observed relatively higher expression levels of some RNL-encoding genes in the

vasculature-related cells. In addition, members in the same RNL gene family exhibited different expression levels across different cell types. For the three *ADR1* homologs, these levels were as follows: *ADR1* had a higher expression in procambium cells and was highly induced in these cells at 40 hpi; *ADR1-L1* had a higher expression in bundle sheath cells and was further induced at both 24 and 40 hpi, and it was also induced by fungal infection in procambium and phloem parenchyma cells but to a lesser extent; and *ADR1-L2* had a higher expression in procambium cells and was induced in procambium, phloem parenchyma, and phloem companion cells (Figure 2B). For the *NRG1* homologs, *NRG1.1* was expressed in epidermal and procambium cells, whereas *NRG1.2* was mainly expressed in procambium cells. Interestingly, the expression of *NRG1.1* was decreased after fungal infection, especially at 40 hpi; on the contrary, *NRG1.2* was strongly induced in procambium cells by fungal infection (Figure 2B). These results suggest potential functional variation in these RNL homologs and imply a fine-tuning in their deployment. The contrasting expression changes in the two *NRG1* homologs might be indicative of a putative pathogen suppression of plant defense-related genes in certain cell type(s).

In contrast to TNL and RNL, we did not observe a general trend of vasculature-enriched expression in genes encoding CNLs, with a few exceptions (Figure 2B). For example, a cluster of CNL genes, including *CW9* and *ZAR1*, showed a relatively higher expression in vasculature cells; *RF9* was predominantly expressed, and further induced by fungal infection, in guard cells; and the transcripts of *SUMM2* was only detected in phloem companion cells at 24 hpi.

We next determined the broad cell-type-specific patterns in the changes of NLR gene expression after fungal infection. For this purpose, we compared the aggregated expression of the three NLR families at 24 and 40 hpi with mock-treated samples across each cell type (Figure 2C). Again, a significant overall induction was observed in all four vasculature-related cell types in TNL-encoding genes after fungal infection. A moderate induction was also observed in mesophyll cells for both TNL- and CNL-encoding genes, but it was absent in epidermis or guard cells. In addition, CNLs, collectively, showed an induction in phloem companion cells at 40 hpi. RNLs also showed a moderate but statistically significant induction in procambium cells at 40 hpi.

We are particularly interested in the vasculature-enriched expression of TNLs. In addition to TNLs, the TIR domain is also present in other proteins. We therefore examined whether the cell-type-specific expression pattern is a unique feature for TIR-NLRs. For this purpose, we generated a phylogenetic tree of TIR domain-containing proteins encoded in the *Arabidopsis* Col-0 genome and mapped the scRNA-seq data (basal expression, without fungal infection) to each gene (Figure 3). The TIR domain-containing proteins can be divided into several groups, including one major group that mostly consists of TNLs (as highlighted in Figure 3). Another group contains both TNLs and non-TNL TIR proteins, and a third group contains more divergent TNLs such as *RRS1*. Interestingly, the vasculature-enriched expression is a feature that is only observed in the first group, which has genes encoding mainly TNLs. Conversely, many genes in the other groups, especially those encoding non-TNLs, were undetectable in our scRNA-seq, indicating relatively low expression levels. More importantly, genes in the other

groups lack a general pattern of vasculature-enriched expression. Taken together, these results revealed cell-type-specific expression of NLRs, especially in TNLs and RNLs, as a previously unknown phenomenon in plant immunity.

We also examined 216 genes putatively encoding cell-surface-embedded RLKs⁴¹ and found that 181 of them were detectable in our scRNA-seq dataset (Table S2D). Interestingly, we observed a positive correlation between the expression patterns of NLR- and RLK-encoding genes in almost all the cell types in mock-treated and infected tissues (Figure S3). This observation suggests a potential coordination among different classes of immune receptors in plant cells.

Spatial heterogeneity of gene expression in correlation to fungal distribution

In the transcriptome atlas, clusters 6 and 18 were special because of the following: (1) they constitute cells predominantly from infected tissues (Figures 1D and S4A); and (2) unlike the other cell clusters, cells in these 2 clusters could not be categorized into a specific cell type. Therefore, cells belonging to these 2 clusters have unique gene expression signatures, likely due to significant transcriptome reprogramming in response to fungal infection. Indeed, using bulk RNA-seq,⁷ we found that these cells were enriched with transcripts from genes that were previously found to be induced by *C. higginsianum* infection (Figure S4B; Table S4A). Using all the cells belonging to these 2 clusters (6,603 in total) as one input, we defined 25 sub-clusters, which were successfully assigned to epidermis, mesophyll, vasculature, or guard cells (Figure S4C; Table S4B). These cells were combined with other cells that have already been classified to each cell type to construct trajectory curves through which the progression of transcriptomic changes in plant cells during infection could be elucidated in a cell-type-specific manner.

Fungal infection is a spatiotemporal dynamic process where only a subset of plant cells comes into direct contact with the pathogen. We deployed a trajectory analysis by capturing gradual gene expression changes that occur during the infection process at single-cell level. For this analysis, the scRNA-seq dataset was partitioned into four groups, each representing a major cell type. These groups were individually subjected to the Monocle method analysis,⁴² through which a pseudotime value was assigned to each cell to indicate their specific state within a continuous process. A trajectory curve for each cell type was then generated. Through a comparative analysis of the trajectory curves of each of the four cell types between mock treatment and fungal infection, a gradual shift toward the pseudotime value of “1” was observed in the cell populations affected by fungal infection (Figure 4A). Specifically, cells from the 24-hpi tissues exhibited enrichment in the middle region of the curve, while cells from the 40-hpi tissues predominantly displayed pseudotime values ranging between 0.5 and 1. This cell population shift with the progression of the fungal infection was also evident when comparing trajectory curves generated by cells from 24-hpi, and 40-hpi samples with the mock-treated samples (Figure 4A).

Considering the observed trend in cell population shifts from mock-treated to infected samples, we hypothesized that pseudotime values represented the spatiotemporal dynamics of plant responses during fungal infection. In line with this hypothesis, we

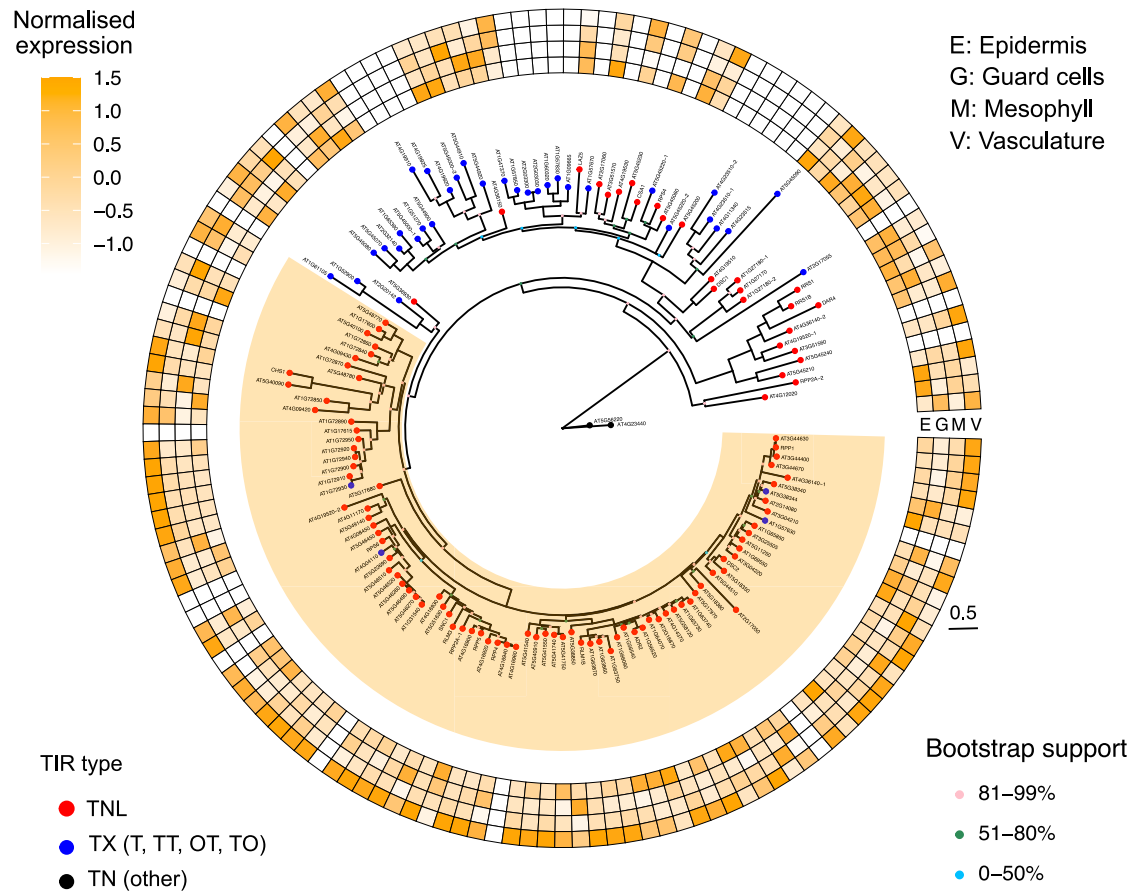


Figure 3. Vasculature-enriched expression is specific to TNLs, not other TIR domain proteins

Gene expression data from non-inoculated samples in four major cell types (E, epidermis; G, guard cells; M, mesophyll; V, vasculature) are mapped onto a phylogenetic tree of TIR domain proteins encoded in the *Arabidopsis* Col-0 genome. The maximum-likelihood phylogeny was built using a 356 aa alignment of the TIR domain. In the case where multiple TIR domains were identified from one protein, the gene name is suffixed with “-1” and “-2.” The scale shows substitutions per site. The heatmap shows relative expression levels normalized for each gene. Undetectable levels are shown as blank. Bootstrap supports below 100% are colors for each node. Each protein is also colored-coded for sub-classes as TNL (red); TX (blue) that includes TIR-only (T), TIR-TIR (TT), other-TIR (OT), and TIR-other (TO); or TN (black) that includes two divergent TIR-PLOOP proteins. The major clade highlighted in orange consists of mostly TNLs that generally showed higher expression in vasculature.

found a clear pattern of gradual increase in the *FRK1* gene expression in cells with pseudotime values increasing from 0.5 toward 1 (Figure 4B). Particularly, cells expressing higher levels of *FRK1* were enriched in the 40-hpi sample. Moreover, cells belonging to clusters 6 and 18 showed a significant enrichment of pseudotime values between 0.5 and 1 and exhibited relatively high *FRK1* expression (Figure 4B). These results confirmed a strong association of clusters 6 and 18 with fungal infection.

FRK1 is a well-established early immune response marker^{43–46} and was reported to be highly induced at the infection sites of powdery mildew, using a laser-microdissection method.³² To establish a relationship between pseudotime values of *Arabidopsis* cells and their relative position to the invading fungal hyphae, we experimentally examined the expression pattern of *FRK1* by using live-cell imaging. In this experiment, leaves of *Arabidopsis* transgenic plants expressing *pFRK1::3xVenus-NLS*⁴³ were inoculated with conidial suspensions of *C. higginsianum*, and *FRK1* expression was monitored by quantifying the intensity of yellow fluorescence at 48 hpi. We used a *C. higginsianum* strain constitutively expressing green

fluorescence,⁴⁷ which allowed for simultaneous detection of the location of the fungus. We found that the yellow fluorescence was specifically accumulated in cells and either had direct contact with or were in close proximity to the fungal hyphae. The strongest yellow fluorescence signals were observed in cells directly colonized by the fungus, and the fluorescence level gradually decreased in the neighboring cells (Figure 4C). This observation suggests that the pseudotime value of a cell reflects its relative position to the invading fungus. Further comparisons with the most significantly induced genes (44 genes with $\log_2|FC| > 20$) at the microdissected infection site of powdery mildew³² revealed a strong correlation with the transcriptomic changes observed in cells with pseudotime values close to 1 in our analysis (Figure 4D; Table S4C). These results support that the dynamic cellular response represented in the trajectory curve mainly reflects a spatial heterogeneity determined by the uneven distribution of the fungal pathogen in the infected tissue.

We next examined the transcriptional signatures in cells in the epidermal trajectory curve and revealed 767 genes

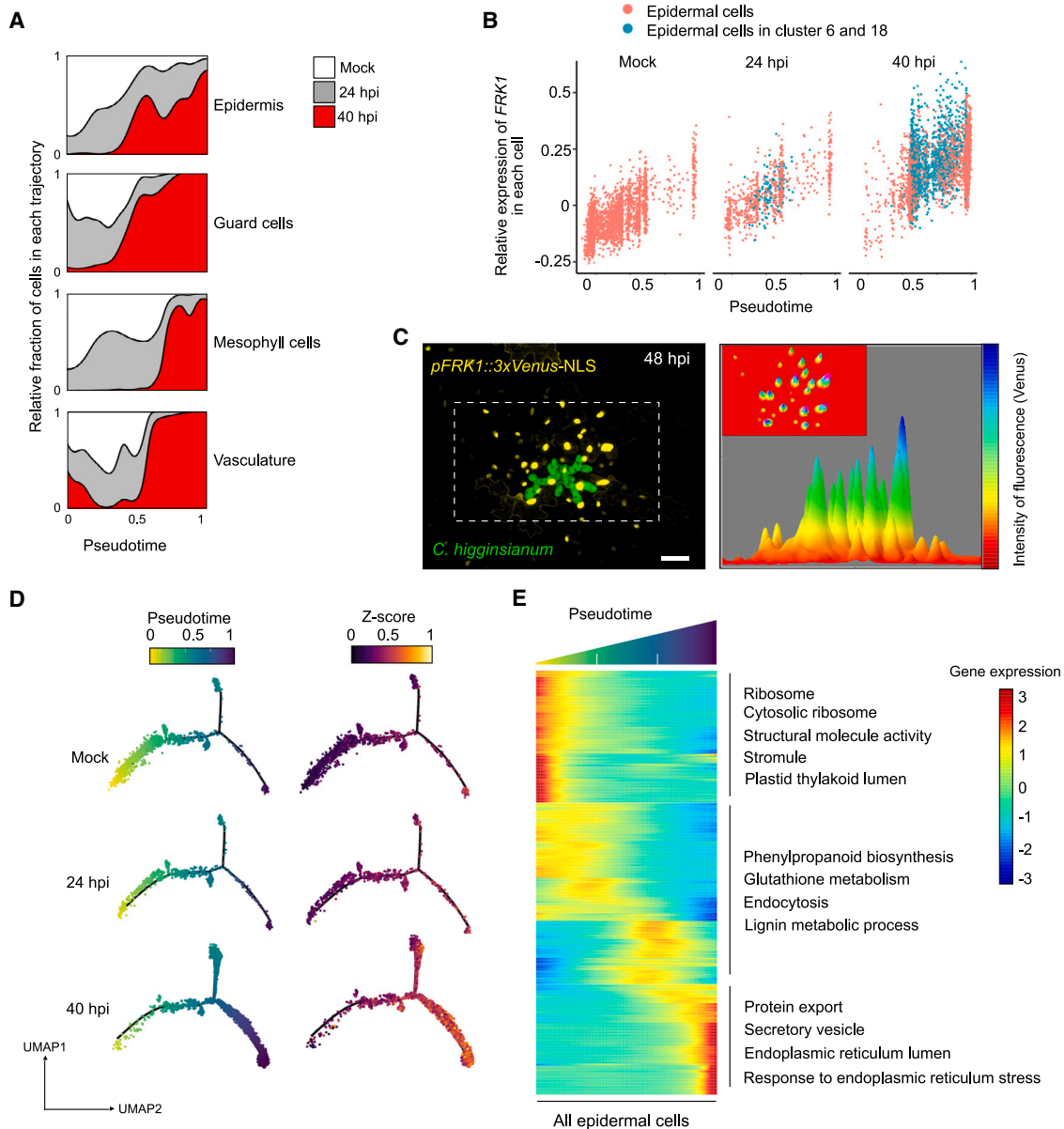


Figure 4. Spatiotemporal heterogeneity of cellular response to fungal distribution

(A) A shift of pseudotime toward “1” in the plant cell populations after fungal infection. Each cell was assigned a pseudotime value based on transcriptional signatures that exhibit gradual changes. The density plots show fractions of cells with different pseudotime values from mock, 24-hpi, or 40-hpi samples in each of the four major cell types.

(B) *FRK1* expression exhibited a gradual increase in epidermal cells with pseudotime values from 0 toward 1. Each dot represents a cell. Blue dots represent cells from clusters 6 and 18 in Figure 1D, which mainly consist of cells from the 40-hpi sample. These cells also had relatively higher levels of *FRK1* expression.

(C) *FRK1* was highly induced in cells that had direct contact with the invading fungus. Transgenic *Arabidopsis* expressing 3xVenus-NLS under the *FRK1* promoter were inoculated with *C. higginsianum* and imaged at 48 hpi. The micrograph shows yellow fluorescence signals of Venus, which indicates the promoter activity of *FRK1*, and green fluorescence, which was expressed in the fungal hyphae. The boxed area was further analyzed by quantifying the Venus signal intensity, which is shown in the plot from a horizontal angle. The mini micrograph shows the same distribution of the Venus signals but from a vertical angle. Scale bars, 15 μ m.

(D) The cell population shift in response to fungal infection correlates with the expression dynamics of genes induced at the infection sites of powdery mildew. Left panel: trajectory curves of epidermal cells from mock, 24-hpi, and 40-hpi samples, with each dot representing a single cell. The color of a dot indicates its pseudotime value. Right panel: aggregated expression level of a set of 44 genes that were identified to be induced at the infection site of powdery mildew³² mapped to the trajectory curves. The color intensity indicates the relative value of module score in the cell.

(E) Different cellular processes are enriched in cell populations that have different pseudotime values. The heatmap shows relative expression levels of pseudotime-dependent genes in the trajectory of epidermal cells, which were grouped into three populations based on hierarchical clustering. Representative KEGG metabolic pathways and gene ontology (GO) terms enriched in each population are highlighted.

that exhibited pseudotime-dependent changes (Figure 4E; Table S4D). Of these, 296 genes were highly expressed in the cells at the beginning of the curve (with pseudotime values close to “0”). None of these genes have known functions related to plant defense. These cells were thus likely distal to the fungal IH, and their transcriptomes were not significantly affected by the infection. Another 329 genes were induced in cells in the middle of the trajectory curve, possibly surrounding the infection sites without direct contact with the fungal hyphae. Some of these genes, such as *KTI1*, *GSTU10*, and *WRKY75*, encode positive regulators of plant defense, suggesting activation of immune response in these cells. Finally, 142 genes were specifically induced in cells at the end of the curve (with pseudotime values close to “1”), which likely had direct interactions with the IH. Among these genes are well-studied immune responsive genes such as *FRK1* and *PEP2*. Enrichment analysis demonstrates that distinctive cellular processes were activated in the different cell populations along the trajectory curve. For example, genes in secretion-related pathways were specifically induced in cells at the infection sites (Figure 4E), consistent with direct involvement of these pathways in antimicrobial activities. These analyses revealed specific cellular processes that were upregulated in response to fungal infection in different plant cell populations based on their relative location with the pathogen.

A guard cell-specific response leads to stomatal closure at the infection sites

Similar to the epidermal cells, the trajectory of guard cells also demonstrated a transcriptome switch in cells with pseudotime values toward 1 after fungal infection, which is correlated with the induced expression of infection site-related genes (Figure 5A). By investigating pseudotime-dependent genes, we discovered pathways associated with propionate metabolism, nitrogen metabolism, and sulfur metabolism, which were specifically induced in guard cells at the infection sites (Figure 5B; Tables S5A and S5B). Sulfur metabolism is well known to be responsive to abscisic acid (ABA), which modulates stomatal closure.⁴⁸ This prompted us to investigate the expression changes of ABA-related genes in the guard cells. A total of 106 ABA-related genes in the *Arabidopsis* genome were analyzed for expression patterns, including 51 positive regulators and 55 negative regulators (Tables S5C and S5D). We observed a strong correlation between the gene expression levels of the positive regulators in guard cells and their pseudotime values. Key genes, such as *PED1*, *CAR8*, and *CPK11*, exhibited a progressive increase in expression in guard cells with pseudotime values trending toward 1, signifying a gradual induction in cells at the infection sites (Figure 5C). Interestingly, an opposite pattern, i.e., gradual decrease, was observed in the expression of genes encoding negative regulators of ABA signaling, such as *ABR1*, *ABI1*, *FER1*, and *GCR1* (Figure 5C). These expression patterns were specific to guard cells, as their expression in the other three cell types remained unchanged (Figure S5). Therefore, ABA signaling seemed to be activated in response to fungal infection in a spatially dynamic and cell-type-specific manner.

ABA is a major regulator of stomatal closure, which is induced to prevent bacterial entry into the leaf apoplast.^{4,49,50} It has also

been observed that open stomata could be exploited by fungi and oomycetes as an alternative entry mechanism and at the later infection stage for sporulation.^{9,51–53} We examined whether the specific activation of ABA signaling led to changes in the stomatal aperture during *C. higginsianum* infection. For this purpose, confocal microscopy was conducted on *Arabidopsis* leaves inoculated with *C. higginsianum* to capture images of guard cells at 40 hpi. The width/length ratio was measured for each stomata by using a machine learning-based imaging acquisition workflow to quantify the aperture.⁵⁴ We measured the stomatal aperture in guard cells at the infection sites, in the more distal but still the neighboring regions of the IH, and in mock-treated tissues. A comparison between these different guard cell populations revealed a decrease in the stomatal opening when the guard cells were in the proximity of the invading pathogen and complete closure when the cells were in direct contact with the fungus (Figure 5D). These results demonstrate a guard cell-specific potentiation of ABA signaling, mediated by the coordinated expression changes of positive and negative regulators, which may result in the closure of stomata.

Activation of GSL biosynthesis at the infection sites employs cell-type-specific gene expression

When comparing the cells at the infection sites to the whole atlas, we found that only 16 genes were induced in all 4 cell types. In contrast, 541, 351, 2, and 20 genes were specifically induced in epidermal, guard, mesophyll, and vasculature cells, respectively (Figure 6A; Table S6A). This result demonstrates strong cell-type-specific changes in gene expression, particularly in epidermal and guard cells. Enrichment analysis of these genes suggests that indole-related biological processes were induced at the infection sites (Figure S6A). Glucosinolate (GSL)-related metabolism plays an important role in pathogen resistance.^{55–57} We found that five out of eight genes in the core GSL pathway, eight out of 14 genes in the indole GSL (IG)-specific pathway, and one out of 15 genes in the aliphatic GSL (AG)-specific pathway were induced at the infection site in at least one cell type (Figure S6B). In addition, tryptophan metabolism and methionine metabolism, which are upstream of IG and AG biosynthesis, respectively,^{58–60} were also induced (Table S6B). Interestingly, many of the GSL-related genes exhibited cell-type-specific expression. For instance, the IG-specific genes encoding *ASA1* (which converts chorismite into indole) and *TSB1* (which converts indole into tryptophan) were induced in epidermis, vasculature, and guard cells but not in mesophyll cells (Figures 6B and 6C). Transcripts of *SUR1* and *SOT16*, encoding components in the core GSL biosynthesis, were enriched in guard cells and vasculature cells at the infection sites but not in epidermal or mesophyll cells (Figure 6C). Furthermore, 9 out of 19 camalexin biosynthetic genes were highly induced at the infection sites, and many of them also showed cell-type-specific induction (Figure S6B). For example, *CYP71A12* and *CYP71A13* both convert indole-3 acetaldoxime (IAOx) into indole-3 acetonitrile; however, *CYP71A12* was induced mainly in the epidermis, whereas *CYP71A13* was almost exclusively induced in the vasculature cells (Figure S6B). The cell-type-specific expression of GSL metabolism-related genes suggests distinct induction of these antimicrobial compounds among different cell types in responses to fungal infection.

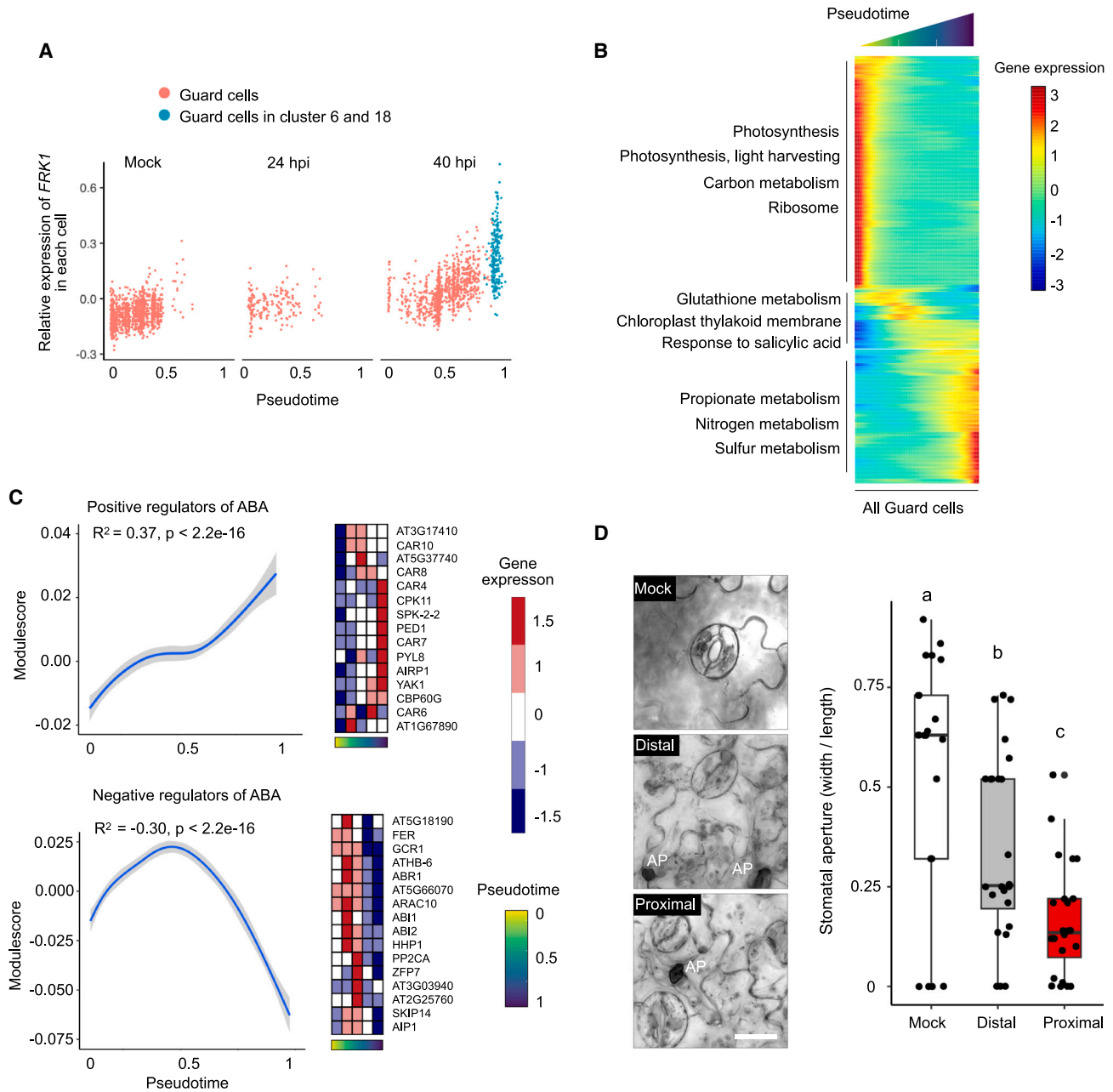


Figure 5. A guard cell-specific response leads to stomatal closure at the fungal infection site

(A) Gradual increase of *FRK1* expression levels in guard cells with pseudotime values from 0 to 1. (B) Different cellular processes are enriched in guard cell populations with different pseudotime values. The heatmap shows relative expression levels of pseudotime-dependent genes along the trajectory curve of all guard cells. Representative GO terms enriched in each cell population are highlighted.

(C) ABA signaling is activated in guard cells with pseudotime values toward “1.” The line plots show linear regression of relative expression levels of genes encoding positive (upper panel) or negative (lower panel) regulators of ABA signaling in guard cells, with the pseudotime values of these cells. The heatmaps show the expression profiles of genes that exhibited the most significant changes.

(D) Stomata closure was observed at the fungal infection sites. Representative micrographs from live-cell imaging show the status of stomatal aperture from the leaves treated with water (mock) or inoculated by *C. higginsianum* at 40 hpi. Fungal appressoria are labeled as “AP.” The “distal” cells were defined as being separated from the fungus by at least one and up to five epidermal cells. The “proximal” cells were defined as being immediately adjacent to fungal appressoria. Scale bars, 10 μ m. Stomatal aperture was measured using the micro-images of guard cells. One-way ANOVA was used to determine the significant differences, which are labeled with different letters. The imaging acquisition was performed at least 3 times for each experiment in two independent experiments.

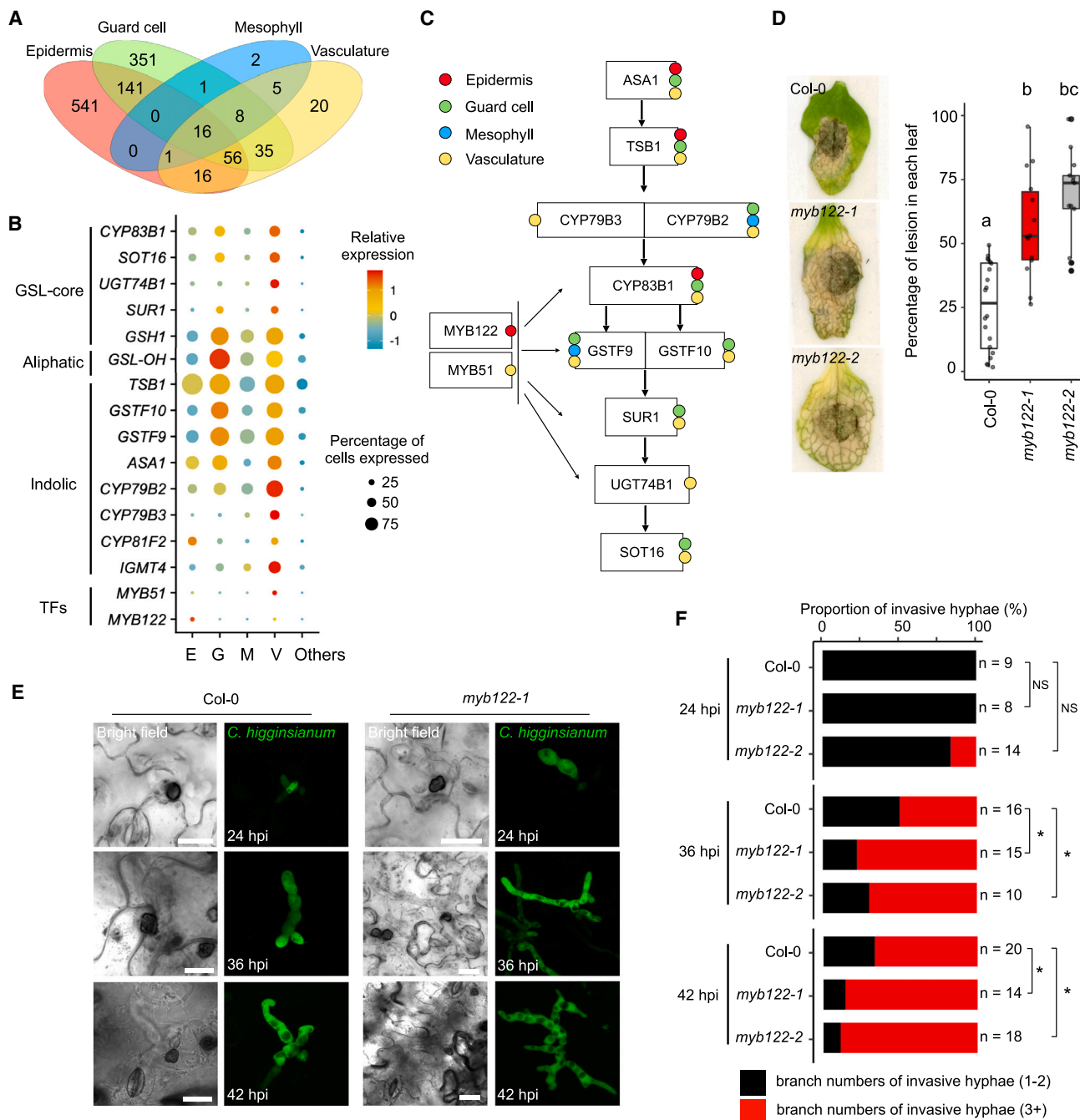


Figure 6. MYB122 was specifically induced in epidermal cells at the fungal infection sites and contributed to resistance

(A) Cell-type-specific gene induction in cells that had direct contact with the invading fungus. The Venn diagram shows the number of induced genes from each of the four major cell types (E, epidermis; G, guard cells; M, mesophyll; V, vasculature) at the infection sites of *C. higginsianum*. The cutoff was set as $\log_2[FC] > 0.25$, $pct.1 > 0.2$, $diff.pct > 0.1$, $p\text{-adj} < 0.05$.

(B) Genes encoding enzymes in the glucosinolate (GSL) pathway were induced in cells at the fungal infection site. *Arabidopsis* genes with proposed functions in the GSL pathway⁵⁵ were analyzed for cell-type-specific activation. Expression profiles of GSL-related genes at the infection sites are plotted in four major cell types. The size of the dots indicates the proportion of cells in which the gene was induced, and the colors indicate relative expression levels.

(C) Cell-type-specific induction of genes involved in indolic glucosinolate (IG) biosynthesis.

(D) Hypersusceptibility of MYB122 mutants to *C. higginsianum*. Two T-DNA insertion mutants of MYB122 were analyzed for susceptibility, compared with wild-type *Arabidopsis* (Col-0). Leaves of 4-week-old *Arabidopsis* plants (wild-type Col-0 and two independent MYB122 mutants) were inoculated by conidial suspensions of *C. higginsianum*. Disease symptoms were monitored at 5 days post inoculation, and the lesion sizes on each inoculated leaf were quantified as the ratio of discolored area vs. total leaf area. Each experiment was repeated at least 3 times. One-way ANOVA was used to determine the significant differences, which are labeled with different letters ($p < 0.05$).

(legend continued on next page)

Three transcription factors were proposed to regulate GSL biosynthesis by regulating the expression of several key enzymes in the pathway^{55,61,62}; however, only *MYB51* and *MYB122* exhibited induction at infection sites. Intriguingly, their expression displayed strong cell-type specificity: *MYB122* was only induced in the epidermis while *MYB51* was only induced in the vasculature cells (Figures 6B, 6C, and S6B). In particular, *MYB122* had not been reported to contribute to plant defense. We determined the significance of *MYB122* induction using two independent transfer DNA (T-DNA) insertion *Arabidopsis* mutants (Figure S6C). Both mutants exhibited enhanced susceptibility to *C. higginsianum* as indicated by the larger lesion sizes on inoculated leaves of adult plants and more severe disease symptoms at 5 days post inoculation (dpi) (Figure 6D). We then performed live-cell imaging to monitor fungal invasive growth in the epidermal cells of *Arabidopsis* leaves inoculated with conidial suspensions of *C. higginsianum* during a time course at 24, 36, and 42 hpi (Figure 6D). We observed that the fungal infection was accelerated in the *myb122* mutant plants compared with wild-type plants (Figure 6E). In particular, the fungal IH tend to develop secondary IH with more branches in the *myb122* mutant plants. Quantification of branched IH in epidermal cells showed significant differences between the *myb122* mutant plants and wild-type plants at 36 and 42 hpi (Figure 6F), suggesting a potential role of *MYB122* in restricting the biotrophic growth of *C. higginsianum*. These results demonstrate a significant contribution of *MYB122* to plant defense, presumably through elevating the production of GSL-related antimicrobial metabolites in epidermal cells at the infection sites. These findings emphasize the recruitment of different sets of genes involved in the induced GSL biosynthesis in different cell types.

DISCUSSION

Single-cell-based omics are powerful tools for constructing the progression of a biological process and understanding the heterogeneity among different cell populations. In recent years, this technology has been applied to plant science, especially in research studying developmental processes,^{37,38,63,64} and more recently, plant-microbe interactions.^{65–67} Here, we generated a single-cell transcriptome atlas with ~95,000 cells during infection by a fungal pathogen that colonizes the leaf tissue of the model plant *Arabidopsis*. This atlas encompasses all major cell types in leaves, allowing for the identification of cell-type-specific cellular responses during fungal invasion. We further assigned infection site-associated cells using trajectory inference and live-cell imaging, which enabled the dissection of the spatio-temporal dynamics of plant response to fungal colonization.

Pathogens utilize diverse mechanisms to enter plant tissue and colonize different organs. Many pathogens can establish infection in the plant vascular system.⁶⁸ We observed that many genes encoding intracellular immune receptors (NLRs) were highly expressed in vasculature-related cells, and in

many cases, they were further induced by fungal infection in these specific cell types. As key components of plant immunity, NLRs recognize pathogen effectors delivered into plant cells and activate defense response. The specific expression of TNLs in procambium cells may indicate a role in defending pathogens that colonize xylem and phloem, such as the bacterial pathogens *Xylella fastidiosa*,⁶⁸ *Xanthomonas* spp.,⁶⁹ phytoplasmas,⁷⁰ *Ralstonia solanacearum*,⁷¹ and *Candidatus Liberibacter* spp.,⁷² as well as the fungal pathogens such as *Fusarium oxysporum*⁷³ and *Verticillium* spp.,⁷⁴ and the oomycete pathogen *Pythium ultimum*.⁷⁵ Most of these pathogens rely on effector proteins to suppress host immune systems. Interestingly, a rapid and localized vascular browning reminiscent of hypersensitive response was found in crucifer plants when they were inoculated with incompatible *Xanthomonas campestris* strains,⁷⁶ indicating potential effector recognition in the vasculature. Indeed, specific effector-NLR recognition in vasculature has been reported. For example, tomato CNL I-2 recognizes the *F. oxysporum* effector Avr2 in the xylem sap.⁷⁷ However, how NLR receptors, and indeed immune signaling, work in the vasculature tissues in general is poorly understood.⁷⁸ The fact that NLR-mediated resistance against the phloem-colonizing bacterial pathogens, such as *Liberibacter* and phytoplasmas, has not been reported indicates that classic ETI may not be deployed in mature vasculature tissues, although these pathogens do secrete effectors.^{70,79} Future research is warranted to experimentally confirm the cell-type-specific expression of NLRs, especially the specific expression of TNLs and RNLs in the vasculature-related cells. Through cis-element analysis, potential transcription factor(s) that may be involved in this regulation can be identified and further functionally characterized to examine the biological significance of this expression pattern in plant immunity.

While NLRs are activated at protein level by forming resistance complexes, some NLRs, particularly many of the TNLs, could be induced at transcription level after the activation of pattern-triggered immunity (PTI)^{21,80} and ETI.⁸¹ Consistently, we found a family of TNLs to be highly induced in phloem companion cells during the early infection stage of *C. higginsianum*, which is not known to colonize vasculature. Therefore, the enhanced expression of TNLs may represent a general response to protect the vasculature organs, which are not only vital for plant growth and survival but could also be hijacked by pathogens for systematic infection. In contrast to TNLs, we did not observe a general cell-type-specific expression pattern for CNLs, which may reflect a functional divergence between these two major classes of NLRs. For example, activated TNLs function as NAD⁺-hydrolyzing enzymes and produce signaling molecules to activate immune response.^{82–84} It will be interesting to investigate whether the NAD⁺ hydrolysis products could be mobile through the vasculature and potentially involved in cell non-autonomous immunity.

A major challenge in the studies of plant-pathogen interactions is the uneven distribution of pathogen invasion/colonization and,

(E) Accelerated progression of fungal infection in the *myb122* mutants. Representative micrographs showing *C. higginsianum* invasive growth in the leaves of wild-type (Col-0) or *myb122-1* plants at 24, 36, and 42 hpi. Scale bars, 10 μ m.

(F) Quantitative analysis showing the accelerated fungal infection in *myb122* mutant plants. Numbers of primary and secondary invasive hyphae (represented by the number of branches) were counted in leaf tissues at 24, 36, and 42 hpi using live-cell images. n = number of images analyzed. T test was performed to determine statistical significance, using data from two biological replicates. ns, not significant, *p < 0.05.

in the case of filamentous pathogens, the dynamic pathogen development in the host tissue.^{10,85,86} We determined the spatiotemporal heterogeneity in plant responses at single-cell resolution. Our analyses revealed a robust correlation between cellular response and the proximity of the cell to the invading fungal hyphae. A similar coupling of spatial and temporal responses was also observed during bacterial infection.⁶ More importantly, we uncovered a cell-type-specific response that showed spatial dynamics. In this case, coordinated expression changes in positive and negative regulators of ABA signaling occurred specifically in guard cells that had direct contact with the fungus. This activation of ABA signaling gradually decreased in surrounding cells and diminished in more distal cells. Consistent with this transcription signature, a gradual decrease in stomatal aperture toward the fungal infection sites was also observed. Stomata formed by guard cells serve as natural entry points for bacterial pathogens.^{3,4} It has been well established that stomatal closure is a defense response induced upon bacterial perception to prevent their entry into the apoplast.^{4,87} Although filamentous pathogens can force their entry through mechanical pressures generated at appressoria (AP)^{8,88} or slicing through the epidermal cells,^{89,90} open stomata could also be exploited as an alternative entry mechanism or at the later infection stage for sporulation by oomycete pathogens.^{9,51} Therefore, the observed stomata closure may be a potential defense response in anticipation of pathogen penetration and/or dissemination. Furthermore, manipulation of stomata has recently been shown to be important for the formation of a nutritious and humid apoplastic environment, which is essential for bacterial proliferation.^{91–93} Therefore, stomatal closure is not only important for pathogen entry but also for disease development. Further functional characterization is required to determine whether and how stomatal closure may regulate fungal infection.

Our work also highlighted the importance of cell-type-specific gene activation in processes important to disease resistance. GSLs are nitrogen- and sulfur-rich phytoanticipins that are critical to plant defense.^{56,94,95} The GSL pathway is activated during immune signaling and has been implicated in resistance against a variety of fungal and oomycete pathogens.^{56,96} Consistent with these previous findings, we observed an overall induction of genes involved in GSL biosynthesis in cells that had direct contact with *C. higginsianum*. Importantly, different genes were specifically induced in different cell types. In particular, *MYB122*, *MYB34*, and *MYB51* were proposed to function redundantly in GSL biosynthesis,⁵⁵ yet we found their specific induction at the infection sites, i.e., in epidermis for *MYB122* and vasculature for *MYB51*. Furthermore, our functional characterization of *MYB122* demonstrated its contribution to restricting fungal biotrophic growth, possibly through specifically regulating the GSL pathways in epidermal cells. These findings exemplify the power of single-cell-based analysis in dissecting gene regulation networks.

In this study, we present a comprehensive single-cell transcriptome atlas in *Arabidopsis* during infection by a hemibiotrophic fungal pathogen, showcasing remarkable gene expression heterogeneity in plant cells. These profiles epitomize the dynamic and complex cellular response to fungal infection, which is influenced not only by cell-type specificity but also by the rela-

tive proximity to fungal invasive growth. This high-resolution transcriptome dataset serves as a valuable resource, primed to catalyze further research aimed at elucidating the molecular intricacies underpinning plant immunity and pathogenesis. We anticipate that investigations on cell-type-specific gene expression and identification of *cis*-elements that regulate these genes will be instrumental in designing constructs for targeted expression of defense-related components in the most relevant plant cells. Facing the urgent need of enhancing disease resistance in crops, these constructs may minimize growth penalty often associated with enhanced immunity, paving the way for the development of more sustainable and resilient agricultural systems.

STAR★METHODS

Detailed methods are provided in the online version of this paper and include the following:

- KEY RESOURCES TABLE
- RESOURCE AVAILABILITY
 - Lead contact
 - Materials availability
 - Data and code availability
- EXPERIMENTAL MODEL AND STUDY PARTICIPANT DETAILS
 - Plant material and growth conditions
 - Growth of *C. higginsianum*
- METHOD DETAILS
 - Inoculation of *C. higginsianum*
 - Microscope for live-cell imaging and stomatal aperture quantification
 - Arabidopsis protoplast preparation for scRNA-seq
 - Single-cell partition and RNA-library construction
 - Alignment of raw scRNA-seq data
 - Quality control, doublet detection, cell-cycle regression, and batch effects removal of scRNA-seq data
 - Clustering and cell type annotation and gene expression analysis in scRNA-seq
 - Phylogenetic analysis of genes encoding TIR-containing proteins
 - Trajectory inference and pseudotime analysis
 - Bulk RNA-seq data analysis
- QUANTIFICATION AND STATISTICAL ANALYSIS

SUPPLEMENTAL INFORMATION

Supplemental information can be found online at <https://doi.org/10.1016/j.chom.2023.08.019>.

ACKNOWLEDGMENTS

We thank Professor Dan MacLean, Dr. Clara Jégousse, and George Deeks for technical support with bioinformatic tools and data management. We are grateful to Professors Richard O'Connell, Jonathan Jones, and Christine Faulkner for kindly providing green fluorescent protein (GFP)-labeled and wild-type *C. higginsianum* strains, respectively. We thank all members of the Ma group for helpful discussions and technical support. This project is supported by Gatsby Charitable Foundation and UKRI BBSRC grant BBS/E/J/000PR9797. P.D. is funded by the European Union, Horizon EU, ERC-2021-StG, R-ELEVATION, 101039824.

AUTHOR CONTRIBUTIONS

W.M. and B.T. conceived the research and designed the experiments. B.T. performed the experiments. B.T., L.F., and M.T.H. analyzed the data. W.M., B.T., and P.D. wrote the manuscript.

DECLARATION OF INTERESTS

The authors declare no competing interests.

Received: April 12, 2023

Revised: July 14, 2023

Accepted: August 29, 2023

Published: September 22, 2023

REFERENCES

- Zhang, J., Coaker, G., Zhou, J.-M., and Dong, X. (2020). Plant immune mechanisms: from reductionistic to holistic points of view. *Mol. Plant* **13**, 1358–1378.
- Lindow, S.E., and Brandl, M.T. (2003). Microbiology of the phyllosphere. *Appl. Environ. Microbiol.* **69**, 1875–1883.
- McLachlan, D.H., Kopischke, M., and Robatzek, S. (2014). Gate control: guard cell regulation by microbial stress. *New Phytol.* **203**, 1049–1063.
- Melotto, M., Underwood, W., Koczan, J., Nomura, K., and He, S.Y. (2006). Plant stomata function in innate immunity against bacterial invasion. *Cell* **126**, 969–980.
- Badel, J.L., Shimizu, R., Oh, H.-S., and Collmer, A. (2006). A *Pseudomonas syringae* pv. *tomato* avrE1/hopM1 mutant is severely reduced in growth and lesion formation in tomato. *Mol. Plant Microbe Interact.* **19**, 99–111.
- Zhu, J., Lolle, S., Tang, A., Guel, B., Kvitko, B., Cole, B., and Coaker, G. (2023). Single-cell profiling of *Arabidopsis* leaves to *Pseudomonas syringae* infection. *Cell Rep.* **42**, 112676.
- O'Connell, R.J., Thon, M.R., Hacquard, S., Amyotte, S.G., Kleemann, J., Torres, M.F., Damm, U., Buiate, E.A., Epstein, L., and Alkan, N. (2012). Lifestyle transitions in plant pathogenic *Colletotrichum* fungi deciphered by genome and transcriptome analyses. *Nat. Genet.* **44**, 1060–1065.
- Wilson, R.A., and Talbot, N.J. (2009). Under pressure: investigating the biology of plant infection by *Magnaporthe oryzae*. *Nat. Rev. Microbiol.* **7**, 185–195.
- Fawke, S., Doumane, M., and Schornack, S. (2015). Oomycete interactions with plants: infection strategies and resistance principles. *Microbiol. Mol. Biol. Rev.* **79**, 263–280.
- Latijnhouwers, M., de Wit, P.J., and Govers, F. (2003). Oomycetes and fungi: similar weaponry to attack plants. *Trends Microbiol.* **11**, 462–469.
- Bozkurt, T.O., and Kamoun, S. (2020). The plant–pathogen haustorial interface at a glance. *J. Cell Sci.* **133**. <https://doi.org/10.1242/jcs.237958>.
- Koeck, M., Hardham, A.R., and Dodds, P.N. (2011). The role of effectors of biotrophic and hemibiotrophic fungi in infection. *Cell. Microbiol.* **13**, 1849–1857.
- Khang, C.H., Berruyer, R., Giraldo, M.C., Kankanala, P., Park, S.-Y., Czymbek, K., Kang, S., and Valent, B. (2010). Translocation of *Magnaporthe oryzae* effectors into rice cells and their subsequent cell-to-cell movement. *Plant Cell* **22**, 1388–1403.
- Spanu, P.D., Abbott, J.C., Amselem, J., Burgis, T.A., Soanes, D.M., Stüber, K., Ver Loren van Themaat, E.V., Brown, J.K., Butcher, S.A., and Gurr, S.J. (2010). Genome expansion and gene loss in powdery mildew fungi reveal tradeoffs in extreme parasitism. *Science* **330**, 1543–1546.
- Ökmen, B., and Doehlemann, G. (2014). Inside plant: biotrophic strategies to modulate host immunity and metabolism. *Curr. Opin. Plant Biol.* **20**, 19–25.
- McDowell, J.M. (2013). Genomic and transcriptomic insights into lifestyle transitions of a hemi-biotrophic fungal pathogen. *New Phytol.* **197**, 1032–1034.
- Münch, S., Lingner, U., Floss, D.S., Ludwig, N., Sauer, N., and Deising, H.B. (2008). The hemibiotrophic lifestyle of *Colletotrichum* species. *J. Plant Physiol.* **165**, 41–51.
- De Silva, D.D., Crous, P.W., Ades, P.K., Hyde, K.D., and Taylor, P.W. (2017). Life styles of *Colletotrichum* species and implications for Plant Biosecurity. *Fungal Biol. Rev.* **31**, 155–168.
- Ngou, B.P.M., Ding, P., and Jones, J.D.G. (2022). Thirty years of resistance: zig-zag through the plant immune system. *Plant Cell* **34**, 1447–1478.
- Dodds, P.N., and Rathjen, J.P. (2010). Plant immunity: towards an integrated view of plant–pathogen interactions. *Nat. Rev. Genet.* **11**, 539–548.
- Bjornson, M., Pimprikar, P., Nürnberger, T., and Zipfel, C. (2021). The transcriptional landscape of *Arabidopsis thaliana* pattern-triggered immunity. *Nat. Plants* **7**, 579–586.
- Aerts, N., Chhillar, H., Ding, P., and Van Wees, S.C.M. (2022). Transcriptional regulation of plant innate immunity. *Essays Biochem.* **66**, 607–620.
- Tsuda, K., and Katagiri, F. (2010). Comparing signaling mechanisms engaged in pattern-triggered and effector-triggered immunity. *Curr. Opin. Plant Biol.* **13**, 459–465.
- Cui, H., Tsuda, K., and Parker, J.E. (2015). Effector-triggered immunity: from pathogen perception to robust defense. *Annu. Rev. Plant Biol.* **66**, 487–511.
- Kourelis, J., Sakai, T., Adachi, H., and Kamoun, S. (2021). RefPlantNLR is a comprehensive collection of experimentally validated plant disease resistance proteins from the NLR family. *PLoS Biol.* **19**, e3001124.
- Gong, Y., Tian, L., Kontos, I., Li, J., and Li, X. (2023). Plant immune signaling network mediated by helper NLRs. *Curr. Opin. Plant Biol.* **73**, 102354. <https://doi.org/10.1016/j.pbi.2023.102354>.
- Mazutis, L., Gilbert, J., Ung, W.L., Weitz, D.A., Griffiths, A.D., and Heyman, J.A. (2013). Single-cell analysis and sorting using droplet-based microfluidics. *Nat. Protoc.* **8**, 870–891.
- Birkenbihl, R.P., Liu, S., and Somssich, I.E. (2017). Transcriptional events defining plant immune responses. *Curr. Opin. Plant Biol.* **38**, 1–9.
- Nobori, T., Velásquez, A.C., Wu, J., Kvitko, B.H., Kremer, J.M., Wang, Y., He, S.Y., and Tsuda, K. (2018). Transcriptome landscape of a bacterial pathogen under plant immunity. *Proc. Natl. Acad. Sci. USA* **115**, E3055–E3064.
- Tsuda, K., and Somssich, I.E. (2015). Transcriptional networks in plant immunity. *New Phytol.* **206**, 932–947.
- Tang, W., Coughlan, S., Crane, E., Beatty, M., and Duvick, J. (2006). The application of laser microdissection to in planta gene expression profiling of the maize anthracnose stalk rot fungus *Colletotrichum graminicola*. *Mol. Plant Microbe Interact.* **19**, 1240–1250.
- Chandran, D., Inada, N., Hather, G., Kleindt, C.K., and Wildermuth, M.C. (2010). Laser microdissection of *Arabidopsis* cells at the powdery mildew infection site reveals site-specific processes and regulators. *Proc. Natl. Acad. Sci. USA* **107**, 460–465.
- Rich-Griffin, C., Eichmann, R., Reitz, M.U., Hermann, S., Woolley-Allen, K., Brown, P.E., Wiwatdirekku, K., Esteban, E., Pasha, A., and Kogel, K.-H. (2020). Regulation of cell type-specific immunity networks in *Arabidopsis* roots. *Plant Cell* **32**, 2742–2762.
- Saelens, W., Cannoodt, R., Todorov, H., and Saeys, Y. (2019). A comparison of single-cell trajectory inference methods. *Nat. Biotechnol.* **37**, 547–554.
- Xu, Z., Wang, Q., Zhu, X., Wang, G., Qin, Y., Ding, F., Tu, L., Daniell, H., Zhang, X., and Jin, S. (2022). Plant Single Cell Transcriptome Hub (PsctH): an integrated online tool to explore the plant single-cell transcriptome landscape. *Plant Biotechnol. J.* **20**, 10–12.

36. Chen, H., Yin, X., Guo, L., Yao, J., Ding, Y., Xu, X., Liu, L., Zhu, Q.-H., Chu, Q., and Fan, L. (2021). PlantscRNAdb: a database for plant single-cell RNA analysis. *Mol. Plant* **14**, 855–857.
37. Lopez-Anido, C.B., Vatén, A., Smoot, N.K., Sharma, N., Guo, V., Gong, Y., Anleu Gil, M.X.A., Weimer, A.K., and Bergmann, D.C. (2021). Single-cell resolution of lineage trajectories in the *Arabidopsis* stomatal lineage and developing leaf. *Dev. Cell* **56**, 1043–1055.e4.
38. Kim, J.-Y., Symeonidi, E., Pang, T.Y., Denyer, T., Weidauer, D., Bezruczyk, M., Miras, M., Zöllner, N., Hartwig, T., and Wudick, M.M. (2021). Distinct identities of leaf phloem cells revealed by single cell transcriptomics. *Plant Cell* **33**, 511–530.
39. Jouannet, V., Brackmann, K., and Greb, T. (2015). (Pro)cambium formation and proliferation: two sides of the same coin? *Curr. Opin. Plant Biol.* **23**, 54–60.
40. De Rybel, B., Mähönen, A.P., Helariutta, Y., and Weijers, D. (2016). Plant vascular development: from early specification to differentiation. *Nat. Rev. Mol. Cell Biol.* **17**, 30–40.
41. Osuna-Cruz, C.M., Paytuyi-Gallart, A., Di Donato, A., Sundesha, V., Andolfo, G., Aiese Cigliano, R., Sanseverino, W., and Ercolano, M.R. (2018). PRGdb 3.0: a comprehensive platform for prediction and analysis of plant disease resistance genes. *Nucleic Acids Res.* **46**, D1197–D1201.
42. Cao, J., Spielmann, M., Qiu, X., Huang, X., Ibrahim, D.M., Hill, A.J., Zhang, F., Mundlos, S., Christiansen, L., and Steemers, F.J. (2019). The single-cell transcriptional landscape of mammalian organogenesis. *Nature* **566**, 496–502.
43. Zhou, F., Emonet, A., Tendon, V.D., Marhavy, P., Wu, D., Lahaye, T., and Geldner, N. (2020). Co-occurrence of damage and microbial patterns controls localized immune responses in roots. *Cell* **180**, 440–453.e18.
44. Asai, T., Tena, G., Plotnikova, J., Willmann, M.R., Chiu, W.-L., Gomez-Gomez, L., Boller, T., Ausubel, F.M., and Sheen, J. (2002). MAP kinase signalling cascade in *Arabidopsis* innate immunity. *Nature* **415**, 977–983.
45. He, P., Shan, L., Lin, N.-C., Martin, G.B., Kemmerling, B., Nürnberger, T., and Sheen, J. (2006). Specific bacterial suppressors of MAMP signaling upstream of MAPKKK in *Arabidopsis* innate immunity. *Cell* **125**, 563–575.
46. Lewis, L.A., Polanski, K., de Torres-Zabala, M., Jayaraman, S., Bowden, L., Moore, J., Penfold, C.A., Jenkins, D.J., Hill, C., and Baxter, L. (2015). Transcriptional dynamics driving MAMP-triggered immunity and pathogen effector-mediated immunosuppression in *Arabidopsis* leaves following infection with *Pseudomonas syringae* pv tomato DC3000. *Plant Cell* **27**, 3038–3064.
47. Birker, D., Heidrich, K., Takahara, H., Narusaka, M., Deslandes, L., Narusaka, Y., Reymond, M., Parker, J.E., and O’Connell, R. (2009). A locus conferring resistance to *Colletotrichum higginsianum* is shared by four geographically distinct *Arabidopsis* accessions. *Plant J.* **60**, 602–613.
48. Batool, S., Uslu, V.V., Rajab, H., Ahmad, N., Waadt, R., Geiger, D., Malagoli, M., Xiang, C.-B., Hedrich, R., and Rennenberg, H. (2018). Sulfate is incorporated into cysteine to trigger ABA production and stomatal closure. *Plant Cell* **30**, 2973–2987.
49. Underwood, W., Melotto, M., and He, S.Y. (2007). Role of plant stomata in bacterial invasion. *Cell. Microbiol.* **9**, 1621–1629.
50. Zeng, W., Melotto, M., and He, S.Y. (2010). Plant stomata: a checkpoint of host immunity and pathogen virulence. *Curr. Opin. Biotechnol.* **21**, 599–603.
51. Wang, Y., Bouwmeester, K., Van de Mortel, J.E., Shan, W., and Govers, F. (2013). A novel *Arabidopsis*–oomycete pathosystem: differential interactions with *Phytophthora capsici* reveal a role for camalexin, indole glucosinolates and salicylic acid in defence. *Plant Cell Environ.* **36**, 1192–1203.
52. Fantozzi, E., Kilaru, S., Gurr, S.J., and Steinberg, G. (2021). Asynchronous development of *Zymoseptoria tritici* infection in wheat. *Fungal Genet. Biol.* **146**, 103504.
53. Ye, W., Munemasa, S., Shinya, T., Wu, W., Ma, T., Lu, J., Kinoshita, T., Kaku, H., Shibuya, N., and Murata, Y. (2020). Stomatal immunity against fungal invasion comprises not only chitin-induced stomatal closure but also chitosan-induced guard cell death. *Proc. Natl. Acad. Sci. USA* **117**, 20932–20942.
54. Sai, N., Bockman, J.P., Chen, H., Watson-Haigh, N., Xu, B., Feng, X., Piechatzek, A., Shen, C., and Gilliam, M. (2023). StomaAI: an efficient and user-friendly tool for measurement of stomatal pores and density using deep computer vision. *New Phytol.* **238**, 904–915.
55. Frerigmann, H., and Gigolashvili, T. (2014). MYB34, MYB51, and MYB122 distinctly regulate indolic glucosinolate biosynthesis in *Arabidopsis thaliana*. *Mol. Plant* **7**, 814–828.
56. Xu, J., Meng, J., Meng, X., Zhao, Y., Liu, J., Sun, T., Liu, Y., Wang, Q., and Zhang, S. (2016). Pathogen-responsive MPK3 and MPK6 reprogram the biosynthesis of indole glucosinolates and their derivatives in *Arabidopsis* immunity. *Plant Cell* **28**, 1144–1162.
57. Widemann, E., Bruinsma, K., Walshe-Roussel, B., Rioja, C., Arbona, V., Saha, R.K., Letwin, D., Zhurov, V., Gómez-Cadenas, A., and Bernards, M.A. (2021). Multiple indole glucosinolates and myrosinases defend *Arabidopsis* against *Tetranychus urticae* herbivory. *Plant Physiol.* **187**, 116–132.
58. Grubb, C.D., and Abel, S. (2006). Glucosinolate metabolism and its control. *Trends Plant Sci.* **11**, 89–100.
59. Gachon, C.M., Langlois-Meurinne, M., Henry, Y., and Saindrenan, P. (2005). Transcriptional co-regulation of secondary metabolism enzymes in *Arabidopsis*: functional and evolutionary implications. *Plant Mol. Biol.* **58**, 229–245.
60. Wang, J.-Z., Li, B., Xiao, Y., Ni, Y., Ke, H., Yang, P., de Souza, A., Bjornson, M., He, X., and Shen, Z. (2017). Initiation of ER body formation and indole glucosinolate metabolism by the plastidial retrograde signaling metabolite, MEcPP. *Mol. Plant* **10**, 1400–1416.
61. Kittipol, V., He, Z., Wang, L., Doheny-Adams, T., Langer, S., and Bancroft, I. (2019). Genetic architecture of glucosinolate variation in *Brassica napus*. *J. Plant Physiol.* **240**, 152988.
62. Harun, S., Abdullah-Zawawi, M.-R., Goh, H.-H., and Mohamed-Hussein, Z.-A. (2020). A comprehensive gene inventory for glucosinolate biosynthetic pathway in *Arabidopsis thaliana*. *J. Agric. Food Chem.* **68**, 7281–7297.
63. Liu, Z., Zhou, Y., Guo, J., Li, J., Tian, Z., Zhu, Z., Wang, J., Wu, R., Zhang, B., and Hu, Y. (2020). Global dynamic molecular profiling of stomatal lineage cell development by single-cell RNA sequencing. *Mol. Plant* **13**, 1178–1193.
64. Shahan, R., Hsu, C.-W., Nolan, T.M., Cole, B.J., Taylor, I.W., Greenstreet, L., Zhang, S., Afanassiev, A., Vlot, A.H.C., and Schiebinger, G. (2022). A single-cell *Arabidopsis* root atlas reveals developmental trajectories in wild-type and cell identity mutants. *Dev. Cell* **57**, 543–560.e9.
65. Cervantes-Pérez, S.A., Thibivilliers, S., Laffont, C., Farmer, A.D., Frugier, F., and Libault, M. (2022). Cell-specific pathways recruited for symbiotic nodulation in the *Medicago truncatula* legume. *Mol. Plant* **15**, 1868–1888.
66. Ye, Q., Zhu, F., Sun, F., Wang, T.-C., Wu, J., Liu, P., Shen, C., Dong, J., and Wang, T. (2022). Differentiation trajectories and biofunctions of symbiotic and un-symbiotic fate cells in root nodules of *Medicago truncatula*. *Mol. Plant* **15**, 1852–1867.
67. Illouz-Eliaz, N., Lande, K., Yu, J., Jow, B., Swift, J., Lee, T., Nobori, T., Castanon, R.G., Nery, J.R., and Ecker, J.R. (2023). Drought recovery induced immunity confers pathogen resistance. <https://doi.org/10.1101/2023.02.27.530256>.
68. Yadeta, K.A., and Thomma, B.P. (2013). The xylem as battleground for plant hosts and vascular wilt pathogens. *Front. Plant Sci.* **4**, 97.
69. Gluck-Thaler, E., Cerutti, A., Perez-Quintero, A.L., Butchacas, J., Roman-Reyna, V., Madhavan, V.N., Shantharaj, D., Merfa, M.V., Pesce, C., and Jauneau, A. (2020). Repeated gain and loss of a single gene modulates the evolution of vascular plant pathogen lifestyles. *Sci. Adv.* **6**, eabc4516.
70. Sugio, A., MacLean, A.M., Kingdom, H.N., Grieve, V.M., Manimekalai, R., and Hogenhout, S.A. (2011). Diverse targets of *Phytoplasma*

- effectors: from plant development to defense against insects. *Annu. Rev. Phytopathol.* **49**, 175–195.
71. Mori, Y., Inoue, K., Ikeda, K., Nakayashiki, H., Higashimoto, C., Ohnishi, K., Kiba, A., and Hikichi, Y. (2016). The vascular plant-pathogenic bacterium *Ralstonia solanacearum* produces biofilms required for its virulence on the surfaces of tomato cells adjacent to intercellular spaces. *Mol. Plant Pathol.* **17**, 890–902.
 72. Wang, N., Pierson, E.A., Setubal, J.C., Xu, J., Levy, J.G., Zhang, Y., Li, J., Rangel, L.T., and Martins, J., Jr. (2017). The *Candidatus Liberibacter*–host interface: insights into pathogenesis mechanisms and disease control. *Annu. Rev. Phytopathol.* **55**, 451–482.
 73. Ma, L.-J., Van Der Does, H.C., Borkovich, K.A., Coleman, J.J., Daboussi, M.-J., Di Pietro, A., Dufresne, M., Freitag, M., Grabherr, M., and Henrissat, B. (2010). Comparative genomics reveals mobile pathogenicity chromosomes in *Fusarium*. *Nature* **464**, 367–373.
 74. Fradin, E.F., and Thomma, B.P. (2006). Physiology and molecular aspects of *Verticillium* wilt diseases caused by *V. dahliae* and *V. albo-atrum*. *Mol. Plant Pathol.* **7**, 71–86.
 75. Levesque, C.A., Brouwer, H., Cano, L., Hamilton, J.P., Holt, C., Huitema, E., Raffaele, S., Robideau, G.P., Thines, M., and Win, J. (2010). Genome sequence of the necrotrophic plant pathogen *Pythium ultimum* reveals original pathogenicity mechanisms and effector repertoire. *Genome Biol.* **11**, 1–22.
 76. Kamoun, S., Kamdar, H.V., Tola, E., and Kado, C.I. (1992). A vascular hypersensitive response: role of the *hrpK* locus. *Mol. Plant Microbe Interact.* **5**, 22–33.
 77. Takken, F., and Rep, M. (2010). The arms race between tomato and *Fusarium oxysporum*. *Mol. Plant Pathol.* **11**, 309–314.
 78. Jiang, Y., Zhang, C.-X., Chen, R., and He, S.Y. (2019). Challenging battles of plants with phloem-feeding insects and prokaryotic pathogens. *Proc. Natl. Acad. Sci. USA* **116**, 23390–23397.
 79. Clark, K., Franco, J.Y., Schwizer, S., Pang, Z., Hawara, E., Liebrand, T.W.H., Pagliaccia, D., Zeng, L., Gurung, F.B., Wang, P., et al. (2018). An effector from the Huanglongbing-associated pathogen targets citrus proteases. *Nat. Commun.* **9**, 1718. <https://doi.org/10.1038/s41467-018-04140-9>.
 80. Tian, H., Wu, Z., Chen, S., Ao, K., Huang, W., Yaghmaiean, H., Sun, T., Xu, F., Zhang, Y., and Wang, S. (2021). Activation of TIR signalling boosts pattern-triggered immunity. *Nature* **598**, 500–503.
 81. Mine, A., Seyfferth, C., Kracher, B., Berens, M.L., Becker, D., and Tsuda, K. (2018). The defense phytohormone signaling network enables rapid, high-amplitude transcriptional reprogramming during effector-triggered immunity. *Plant Cell* **30**, 1199–1219.
 82. Jacob, P., Hige, J., Song, L., Bayless, A., Russ, D., Bonardi, V., El Kasmi, F., Wunsch, L., Yang, Y., and Fitzpatrick, C.R. (2023). Broader functions of TIR domains in Arabidopsis immunity. *Proc. Natl. Acad. Sci. USA* **120**, e2220921120.
 83. Tian, L., Lu, J., and Li, X. (2022). Differential requirement of TIR enzymatic activities in TIR-type immune receptor SNC1-mediated immunity. *Plant Physiol.* **190**, 2094–2098.
 84. Wan, L., Essuman, K., Anderson, R.G., Sasaki, Y., Monteiro, F., Chung, E.-H., Osborne Nishimura, E., DiAntonio, A., Milbrandt, J., and Dangel, J.L. (2019). TIR domains of plant immune receptors are NAD^+ -cleaving enzymes that promote cell death. *Science* **365**, 799–803.
 85. Lo Presti, L., Lanver, D., Schweizer, G., Tanaka, S., Liang, L., Tollot, M., Zuccaro, A., Reissmann, S., and Kahmann, R. (2015). Fungal effectors and plant susceptibility. *Annu. Rev. Plant Biol.* **66**, 513–545.
 86. Giraldo, M.C., and Valent, B. (2013). Filamentous plant pathogen effectors in action. *Nat. Rev. Microbiol.* **11**, 800–814.
 87. Lovelace, A.H., and Ma, W. (2022). How do bacteria transform plants into their oasis? *Cell Host Microbe* **30**, 412–414.
 88. Ryder, L.S., Cruz-Mireles, N., Molinari, C., Eisermann, I., Eseola, A.B., and Talbot, N.J. (2022). The appressorium at a glance. *J. Cell Sci.* **135**, jcs259857.
 89. Bronkhorst, J., Kasteel, M., van Veen, S., Clough, J.M., Kots, K., Buijs, J., van der Gucht, J., Ketelaar, T., Govers, F., and Sprakel, J. (2021). A slicing mechanism facilitates host entry by plant-pathogenic *Phytophthora*. *Nat. Microbiol.* **6**, 1000–1006.
 90. Bronkhorst, J., Kots, K., de Jong, D., Kasteel, M., van Boxmeer, T., Joemmanbaks, T., Govers, F., van der Gucht, J., Ketelaar, T., and Sprakel, J. (2022). An actin mechanostat ensures hyphal tip sharpness in *Phytophthora infestans* to achieve host penetration. *Sci. Adv.* **8**, eabo0875.
 91. Hu, Y., Ding, Y., Cai, B., Qin, X., Wu, J., Yuan, M., Wan, S., Zhao, Y., and Xin, X.-F. (2022). Bacterial effectors manipulate plant abscisic acid signaling for creation of an aqueous apoplast. *Cell Host Microbe* **30**, 518–529.e6.
 92. Roussin-Léveillé, C., Lajeunesse, G., St-Amand, M., Veerapen, V.P., Silva-Martins, G., Nomura, K., Brassard, S., Bolaji, A., He, S.Y., and Moffett, P. (2022). Evolutionarily conserved bacterial effectors hijack abscisic acid signaling to induce an aqueous environment in the apoplast. *Cell Host Microbe* **30**, 489–501.e4.
 93. Gentzel, I., Giese, L., Ekanayake, G., Mikhail, K., Zhao, W., Cocuron, J.-C., Alonso, A.P., and Mackey, D. (2022). Dynamic nutrient acquisition from a hydrated apoplast supports biotrophic proliferation of a bacterial pathogen of maize. *Cell Host Microbe* **30**, 502–517.e4.
 94. Yang, L., Zhang, Y., Guan, R., Li, S., Xu, X., Zhang, S., and Xu, J. (2020). Co-regulation of indole glucosinolates and camalexin biosynthesis by *CPK5/CPK6* and *MPK3/MPK6* signaling pathways. *J. Integr. Plant Biol.* **62**, 1780–1796.
 95. Miękus, N., Marszałek, K., Podlacha, M., Iqbal, A., Puchalski, C., and Świergiel, A.H. (2020). Health benefits of plant-derived sulfur compounds, glucosinolates, and organosulfur compounds. *Molecules* **25**, 3804.
 96. Li, B., Gaudinier, A., Tang, M., Taylor-Teeple, M., Nham, N.T., Ghaffari, C., Benson, D.S., Steinmann, M., Gray, J.A., and Brady, S.M. (2014). Promoter-based integration in plant defense regulation. *Plant Physiol.* **166**, 1803–1820.
 97. O’Connell, R., Herbert, C., Sreenivasaprasad, S., Khatib, M., Esquerré-Tugayé, M.-T., and Dumas, B. (2004). A novel *Arabidopsis*–*Colletotrichum* pathosystem for the molecular dissection of plant-fungal interactions. *Mol. Plant Microbe Interact.* **17**, 272–282.
 98. Hao, Y., Hao, S., Andersen-Nissen, E., Mauck, W.M., III, Zheng, S., Butler, A., Lee, M.J., Wilk, A.J., Darby, C., and Zager, M. (2021). Integrated analysis of multimodal single-cell data. *Cell* **184**, 3573–3587.e29.
 99. Trapnell, C., Cacchiarelli, D., Grimsby, J., Pokharel, P., Li, S., Morse, M., Lennon, N.J., Livak, K.J., Mikkelsen, T.S., and Rinn, J.L. (2014). The dynamics and regulators of cell fate decisions are revealed by pseudotemporal ordering of single cells. *Nat. Biotechnol.* **32**, 381–386.
 100. Korsunsky, I., Millard, N., Fan, J., Slowikowski, K., Zhang, F., Wei, K., Baglaenko, Y., Brenner, M., Loh, P.-R., and Raychaudhuri, S. (2019). Fast, sensitive and accurate integration of single-cell data with Harmony. *Nat. Methods* **16**, 1289–1296.
 101. McGinnis, C.S., Murrow, L.M., and Gartner, Z.J. (2019). DoubletFinder: doublet detection in single-cell RNA sequencing data using artificial nearest neighbors. *Cell Syst.* **8**, 329–337.e4. e324.
 102. Bolger, A., and Giorgi, F. (2014). Trimmomatic: A flexible read trimming tool for Illumina NGS data. *Bioinformatics* **30**, 2114–2120.
 103. Yu, G., Wang, L.-G., Han, Y., and He, Q.-Y. (2012). clusterProfiler: an R package for comparing biological themes among gene clusters. *Omic J. Integr. Biol.* **16**, 284–287.
 104. Bray, N.L., Pimentel, H., Melsted, P., and Pachter, L. (2016). Near-optimal probabilistic RNA-seq quantification. *Nat. Biotechnol.* **34**, 525–527.
 105. Love, M.I., Huber, W., and Anders, S. (2014). Moderated estimation of fold change and dispersion for RNA-seq data with DESeq2. *Genome Biol.* **15**, 550.

106. Leek, J.T., Johnson, W.E., Parker, H.S., Jaffe, A.E., and Storey, J.D. (2012). The sva package for removing batch effects and other unwanted variation in high-throughput experiments. *Bioinformatics* 28, 882–883.
107. Yoo, S.-D., Cho, Y.-H., and Sheen, J. (2007). Arabidopsis mesophyll protoplasts: a versatile cell system for transient gene expression analysis. *Nat. Protoc.* 2, 1565–1572.
108. Cunningham, F., Allen, J.E., Allen, J., Alvarez-Jarreta, J., Amode, M.R., Armean, I.M., Austine-Orimoloye, O., Azov, A.G., Barnes, I., and Bennett, R. (2022). Ensembl 2022. *Nucleic Acids Res.* 50, D988–D995.
109. Berardini, T.Z., Reiser, L., Li, D., Mezheritsky, Y., Muller, R., Strait, E., and Huala, E. (2015). The Arabidopsis information resource: making and mining the “gold standard” annotated reference plant genome. *Genesis* 53, 474–485.
110. Apweiler, R., Attwood, T.K., Bairoch, A., Bateman, A., Birney, E., Biswas, M., Bucher, P., Cerutti, L., Corpet, F., Croning, M.D., et al. (2001). The InterPro database, an integrated documentation resource for protein families, domains and functional sites. *Nucleic Acids Res.* 29, 37–40.
111. Thompson, J.D., Higgins, D.G., and Gibson, T.J. (1994). Clustal W: improving the sensitivity of progressive multiple sequence alignment through sequence weighting, position-specific gap penalties and weight matrix choice. *Nucleic Acids Res.* 22, 4673–4680.
112. Minh, B.Q., Schmidt, H.A., Chernomor, O., Schrempf, D., Woodhams, M.D., von Haeseler, A., and Lanfear, R. (2020). IQ-TREE 2: New models and efficient methods for phylogenetic inference in the genomic era. *Mol. Biol. Evol.* 37, 1530–1534. <https://doi.org/10.1093/molbev/msaa015>.
113. Yu, G. (2020). Using ggtree to visualize data on tree-like structures. *Curr. Protoc. Bioinform.* 69, e96.
114. Sonesson, C., Love, M.I., and Robinson, M.D. (2015). Differential analyses for RNA-seq: transcript-level estimates improve gene-level inferences. *F1000Res* 4, 1521.

STAR★METHODS

KEY RESOURCES TABLE

REAGENT or RESOURCE	SOURCE	IDENTIFIER
Chemicals, peptides, and recombinant proteins		
Cellulase R-10	Yakult	N/A
Macerozyme R-10	Yakult	N/A
Mannitol	Sigma	M1902
Phosphate buffered saline (PBA)	Sigma	P5493-1L
Critical commercial assays		
HiScript® II 1st Strand cDNA Synthesis Kit	Vazyme	Cat# R211-01/02
30 µm cell strainers	Miltenyi Biotec	Cat# 130-098-458
RNeasy Plant Mini Kit	QIAGEN	Cat# 74904
Deposited data		
scRNA-seq and bulk RNA-seq datasets	This study	PRJEB61052
Published dataset	O'Connell et al. ⁷	PRJNA148307
Experimental models: Organisms/strains		
<i>Arabidopsis thaliana</i> : Col-0	ABRC (Arabidopsis Biological Resource Center)	CS70000
<i>Arabidopsis</i> : pFRK1::NLS-3xmVenus	Zhou et al. ⁴³	CS2110219
<i>Arabidopsis</i> : AT3G25800 T-DNA line: <i>myb122-1</i>	ABRC	Salk_027525
<i>Arabidopsis</i> : AT3G25800 CRISPR line: <i>myb122-2</i>	ABRC	Salk_027085
<i>Colletotrichum higginsianum</i>	O'Connell et al. ⁹⁷	IMI 349061
<i>Colletotrichum higginsianum</i> (constitutively expressing GFP)	O'Connell et al. ⁹⁷	IMI 349061
Oligonucleotides		
MYB122_qRT_F: ACCTCTCGAATCTCCCATC	This study	N/A
MYB122_qRT_R: AACTTCATTGATCGGCGTCAC	This study	N/A
SALK_027525_LP: GAAGACCAAAGCTTATCGCC	This study	N/A
SALK_027525_RP: TCCAAACAAGACTCAACGGAC	This study	N/A
SALK_027085_LP: AGCAGAAGGGTTGAAGAAAGG	This study	N/A
SALK_027085_RP: GGGGAGATTCTGAAGAGGTATG	This study	N/A
Software and algorithms		
Seurat	Hao et al. ⁹⁸	https://satijalab.org/seurat/
monocle	Trapnell et al. ⁹⁹	http://cole-trapnell-lab.github.io/monocle-release/
Monocle3	Cao et al. ⁴²	http://cole-trapnell-lab.github.io/monocle-release/monocle3/
Harmony	Korsunsky et al. ¹⁰⁰	https://github.com/immunogenomics/harmony
DoubletFinder	McGinnis et al. ¹⁰¹	https://github.com/chris-mcginnis-ucsf/DoubletFinder
Trimmomatic	Bolger and Giorgi ¹⁰²	https://github.com/usadellab/Trimmomatic
Cellranger	10x Genomics	https://github.com/10XGenomics/cellranger
ClusterProfiler	Yu et al. ¹⁰³	https://guangchuangyu.github.io/software/clusterProfiler/
SAI	Sai et al. ⁵⁴	https://github.com/xdynamics/sai-app
kallisto	Bray et al. ¹⁰⁴	https://pachterlab.github.io/kallisto/

(Continued on next page)

Continued

REAGENT or RESOURCE	SOURCE	IDENTIFIER
DESeq2	Love et al. ¹⁰⁵	https://bioconductor.org/packages/release/bioc/vignettes/DESeq2/inst/doc/DESeq2.html
sva	Leek et al. ¹⁰⁶	https://bioconductor.org/packages/devel/bioc/vignettes/sva/inst/doc/sva.pdf
NLRtracker	Kourelis et al. ²⁵	https://github.com/slt666666/NLRtracker https://github.com/TeamMacLean/nlrsnake
Original code	This study	https://doi.org/10.5281/zenodo.8282688

RESOURCE AVAILABILITY

Lead contact

Further information and requests for resources and reagents should be directed to and will be fulfilled by the lead contact, Wenbo Ma (wenbo.ma@tsl.ac.uk).

Materials availability

Seeds of *Arabidopsis thaliana* plants used in this study were acquired from Arabidopsis Biological research center (ABRC, stock number: see [key resources tables](#)). This study did not generate new unique reagents. *C. higginsianum* strains can be available upon request by contacting the [lead contact](#), Wenbo Ma (wenbo.ma@tsl.ac.uk).

Data and code availability

- The raw data of scRNA-seq and bulk RNA-seq experiments have been deposited in ENA with project ID PRJEB61052 and are publicly available as of the date of publication.
- All the original code is available at Zenodo (<https://doi.org/10.5281/zenodo.8282688>).
- Any additional information required to reanalyze the data reported in this paper is available from the [lead contact](#) upon request.

EXPERIMENTAL MODEL AND STUDY PARTICIPANT DETAILS

Plant material and growth conditions

Arabidopsis thaliana ecotype Col-0 (wild-type) seeds were sterilized and grown on Murashige-Skoog medium plates supplemented with 1% sucrose and 0.8% Phytigel in a growth chamber under 16/8-hour light/dark condition at 22 °C. After 14 days, the seedlings were inoculated with conidial suspensions of *C. higginsianum* and used for scRNA-seq. For pathogenicity assays, Arabidopsis plants were grown in a growth room at 22 °C with 16/18-hour light/dark regime.

Growth of *C. higginsianum*

Growth of *C. higginsianum* was performed as previously described.⁹⁷ *C. higginsianum* strain IMI 349061 was sub-cultured from -80°C stock and grown on PDA plates at 25°C with a 12-hour light-dark cycle. After 5 days, conidia of *C. higginsianum* were harvested by washing with water. The suspension was then used to make a conidial suspension containing 0.2% gelatin at a concentration of 1 x 10⁵ conidia per mL for inoculation.

METHOD DETAILS

Inoculation of *C. higginsianum*

For the scRNA-seq and protoplast isolation, 14-day-old Arabidopsis seedlings were spray-inoculated with either the conidial suspension or 0.2% gelatin as the mock control. The inoculated plants were kept in a growth chamber at 25°C with a 12-hour light-dark cycle. Arabidopsis mutant lines of *myb122* were ordered from SALK (Salk_027525 and Salk_27085) and verified by PCR and qRT-PCR. The primers used to genotype and test gene expression of these mutants are listed in the [key resources table](#). To perform the pathogenicity assay, four-week-old Arabidopsis plants were inoculated with the conidial suspension, and 20 µL conidial suspension was applied to the abaxial side of each adult rosette leaf. The plants were kept at high humidity in a growth chamber under a 12-hour light-dark cycle for five days. Inoculated leaves were collected and immediately scanned. The discolored area (DA) and total area (TA) of each leaf were determined by the Image-Adjust-Color Threshold functions of the ImageJ-fuji software. The lesion size is represented by DA/TA.

Microscope for live-cell imaging and stomatal aperture quantification

The inoculated leaves were collected from seedling tissues after infection unless otherwise specified. The fluorescence signal was observed under a Leica TCL SP8 confocal microscope. A laser of 488-nm wavelength was used for excitation, and an emission

wavelength of 500-nm to 530-nm was used to observe the GFP signal constitutively expressed in *C. higginsianum*. To acquire the Venus signal, a 514-nm laser was used for excitation, and the emission detection wavelength was between 515-nm and 545-nm. To measure stomatal aperture, leaves from 14-day-old seedlings were treated with either water containing 0.1% gelatin for the mock samples or a suspension of fungal conidia for the infected samples. The samples were left in a controlled environment under 16/8-hour light/dark condition at 22°C. At 40 hpi, the samples were collected for imaging acquisition. The image files capturing the stomatal aperture of uninfected, distant, or proximity guard cells were fed into a machine learning-based analysis pipeline.⁵⁴ The width and length of each guard cell were measured and collected for comparison.

Arabidopsis protoplast preparation for scRNA-seq

Before sample collection, live-cell imaging was performed to monitor the robustness of the infection. Protoplast isolation from plant leaves was mainly performed as described¹⁰⁷ with minor modification. Briefly, the mock and infected leaves were cut into 0.5 mm strips and immediately transferred into protoplast enzyme solution (4% cellulase R10, 1.5% macerozyme R10, 0.4 M mannitol, 10 mM KCl, 10 mM CaCl₂, 0.2 M 4-morpholineethanesulfonic acid, and 0.1% BSA). At least 20 leaves of each sample were collected and bulked for further experiments. To shorten the digestion time, the leaf strips were wrapped in foil to avoid light and gently vacuum infiltrated for 20 min, which enabled cell release from seedlings faster than usual. After 1-hour of digestion at room temperature, the leaves were fully digested. The protoplast was filtered via 30 μm cell strainers (Miltenyi Biotec, [key resources table](#)) and washed 2 times with pre-cooled 10% PBS buffer (Sigma, [key resources table](#)) at 4°C in a 50 mL sterile tube. The samples were centrifuged at 150 x g for 2 min at 4°C and then transferred onto ice. The suspension was kept on ice for at least 10 min to allow the protoplasts to fall to the bottom of the tube so that the upper supernatant could be discarded without disturbing the protoplasts. The viability of protoplasts and presence of cell debris was determined by trypan blue staining. The samples with > 90% viability was adjusted to ~ 2000 cells / μL using a hemocytometer. At least four technical replicates for each biological replicate were prepared, and the best two were selected for further single-cell partition.

Single-cell partition and RNA-library construction

The protoplast suspensions were diluted to 1500 cell per μL and immediately loaded into a Chromium Single Cell Instrument (10x Genomics, Pleasanton, CA) to produce single-cell GEMs (Gel Bead-in Emulsions). scRNA-seq libraries were generated using the Chromium Single Cell 3' Gel Bead and Library Kit V3.1 (10x Genomics, Pleasanton, CA). The experiment was performed according to the user's guide provided by the vendor. Eleven cycles of PCR were used to perform cDNA amplification and a further eleven cycles for the final library construction. The libraries were sequenced by Illumina NovaSeq (Novo Gene, Cambridge, UK) to produce paired-end 150 bp reads after quality control by Agilent 2100 Bioanalyzer.

Alignment of raw scRNA-seq data

Reference files for the Arabidopsis genome (TAIR) were downloaded from the Ensembl database.¹⁰⁸ The “cellranger mkref” function (part of Cellranger (V6.0.1), 10x Genomics, Pleasanton, CA) was used to build references. Raw reads were aligned against the genome using Cellranger with default settings. The percentage of aligned reads ranged from 70% to 95% across the samples.

Quality control, doublet detection, cell-cycle regression, and batch effects removal of scRNA-seq data

The downstream analysis was conducted by deploying scripts modified from Seurat (v4.0).⁹⁸ Read10x was used to load raw matrix files, and the function “CreateSeuratObject” was used to build individual Seurat datasets after the Cellranger alignment. To filter out low-quality data, cells with less than 200 genes were discarded, and the genes present in less than three cells were not considered. The dataset was then normalised by “SCTransform” function and fed into Douletfinder workflow to identify doublets during the single-cell partition experiment.¹⁰¹ Briefly, the function “DoubletFinder_v3” was used to determine homotypic doublets with parameters of nExp = round(0.05*nrow(x)) (the number of expected real doublets), pN = 0.25 (the number of artificial doublets), and pK = 0.09 (the neighborhood size). The proportion of artificial neighbors for each cell was calculated and thereby used to define doublet predictions. The resultant cells annotated as “Singlets” in each library were kept for further analysis. The proportion of read counts aligned to chloroplast, mitochondrial, and protoplast-induced genes in each library were investigated before further analysis. Cells with less than 1% of transcripts aligning to mitochondrial and chloroplast genes were taken to further analysis. Further quality control was subsequently performed as low-quality cells were defined as expressing less than 500 genes or more than 50,000 genes. The libraries were then merged using Seurat. To mitigate the effects of cell cycle heterogeneity on cell clustering, genes related to G1-S, and G2-M were identified from a public database¹⁰⁹ and fed into the function “CellCycleScoring”. For normalization, the SCTransform was applied with “var.to.regress” for cell cycle genes regression. The resultant dataset was fed into “RunHarmony” function using seurat dataset assay as “SCT” to correct batch effects between the replicates and samples which generated an integrated Seurat dataset.¹⁰⁰

Clustering and cell type annotation and gene expression analysis in scRNA-seq

Clustering analysis was performed using RunPCA with npc = 30, following RunUMAP and RunTSNE. After this, the cell clusters were identified using functions “FindNeighbors” with parameters k.param = 10, dims = 1:30, and “FindClusters” with a resolution of 0.4. To define genes enriched in each cluster, the “FindAllMarkers” function was used with parameters logfc.threshold = 0.4, min.pct = 0.1, min.diff.pct = 0.1. The Wilcoxon Rank Sum test method was used to define differentially expressed genes between each cluster

and all other cells. The resultant genes were then merged with published single-cell marker genes database^{35,36} and supplementary data from previous studies using Arabidopsis leaf tissue.^{37,38} The resultant genes were used for cell type annotation of each cluster. To visualise and profile marker gene expression, the “Featureplot” function was applied. For further sub-clustering analysis of cluster 6 and 18, the cells were extracted and processed by RunUMAP with a resolution of 0.8 to yield a higher number of clusters. The sub-cluster enriched genes and cell type annotations were performed as described above. To define relative expression of putative and known NLR-encoding genes in Arabidopsis, NLR genes were identified using NLRtracker.²⁵ Only genes with 500 or more normalized UMI counts across the atlas were kept for further investigations. To determine cell type-specific expression, the UMI count matrix generated from Seurat was pulled out. The relative expression of each gene in each cell type was calculated by creating a matrix with aggregated expression values for predefined cell groups using “aggregate_gene_expression” in monocle3.⁴² The expression values were normalized via dividing them by cell size factors. To investigate the expression pattern of CNL, TNL, and RNL gene family, the NLR-encoding genes for each sub-family were pooled together as input for the “AddModuleScore” function in Seurat.⁹⁸ This method defined relative contribution of the targeted gene families to each cell transcriptome. Here, we deployed scripts with default setting “ctrl = 50” as 50 randomly picked genes for benchmarking.

Phylogenetic analysis of genes encoding TIR-containing proteins

To identify genes encoding TIR-containing proteins, NLRtracker²⁵ was ran with default settings against the Arabidopsis proteome (TAIR10). Proteins labelled as TIR were extracted and the longest possible protein sequence with multiple splice variants was obtained using bash scripting. Interproscan v.5.45¹¹⁰ was then used to predict TIR domain locations for 140 proteins. Bash scripting was utilized to extract the longest hit to TIR domain in each protein sequence, and where necessary determine if there were multiple non-overlapping hits per protein and separate these. This meant the total number of TIRs was 147. All 147 Arabidopsis TIR domains were then aligned using ClustalW v.2.1¹¹¹ to create a 356 aa alignment. IQTREE v.2.0.4,¹¹² with model selection via ModelFinder, was used to create a Maximum-Likelihood phylogeny with the model JTT+F+G4 and 1000 bootstrap replicates. The tree was plotted using ggtree¹¹³ with accession information from NLRTracker annotated. Expression data in non-inoculated samples (normalised per gene) across the four cell types was displayed as a heatmap.

Trajectory inference and pseudotime analysis

To construct a trajectory, cells annotated with the same cell type were pooled together and fed into a monocle pipeline.⁹⁹ First, the UMI count matrix for the four major cell types as “single.cell.experiment” was used to construct the dataset by the “newCellDataSet” function, respectively. The resultant dataset was processed to identify genes that were differentially expressed while eliminating batch effects from replicates. The top 2,000 significantly altered genes (according to the q-values) from this dataset were selected for further analysis. To minimize the impact of cell type developmental effects on infection-related trajectory construction, uninfected cells were isolated from each dataset, and wild-type pseudotime was inferred to identify the top 100 significantly altered genes that are potentially crucial for cell type development and determinant. The first set of genes, excluding those identified in the cell type pseudotime analysis, was selected to construct the infection-responsive trajectory, which is vital to build the trajectory elucidating the dynamics of cellular responses to infection. To build the trajectory, the “setOrderingFilter” function was applied and the “DDRTree” method was used to order the cells according to the expression pattern of selected genes. The resultant pseudotime values for four cell types (epidermis, guard cells, mesophyll, and vasculature) were then defined. To assemble a list of genes associated with ABA signaling, genes associated with GO terms “positive regulation of abscisic acid-activated signalling pathway” (GO:0009789) or “negative regulation of abscisic acid-activated signalling pathway” (GO:0009788) were extracted from the TAIR database.¹⁰⁹ The resultant gene lists were input into “AddModuleScore”, and the relative expression of ABA-related genes in each cell was extracted. To define genes enriched at infection sites, the cells with the top 20% pseudotime defined from the trajectory of each cell type was pulled out and defined as infection sites. After that the “FindAllMarkers” function in Seurat was applied to define genes enriched in the cells at infection sites by settings with $\log_2|FC| > 0.25$, $pct.1 \geq 0.2$, $pct.2 < 0.1$, $min.diff.pct > 0.2$, using The Wilcoxon Rank Sum test method. The differentially expression genes were determined by the “FindallMarker” function by using the same cut-off as above. All the enrichment analysis was performed using clusterProfiler package¹⁰³ with cut-offs of q-value < 0.2 for KEGG metabolic pathways and q-value < 0.05 for GO terms.

Bulk RNA-seq data analysis

To determine transcriptome changes in Arabidopsis during the infection by *C. higginsianum*, we downloaded raw RNA-seq datasets PRJNA148307 from a previous study.⁷ The raw reads were processed for quality checking and adaptor removal by Trimmomatic.¹⁰² Trimmed reads were aligned against the Arabidopsis genome using Kallisto¹⁰⁴ followed by tximport¹¹⁴ to generate a count matrix. Batch effects removal was performed by the sva package.¹⁰⁶ Sample size factors, normalization, and differentially expressed genes were analyzed by DESeq2.¹⁰⁵ To identify Arabidopsis genes specifically induced during fungal infection, genes showing $\log_2|FC| > 2$, $p\text{-adj} < 0.05$, and averaged TPM < 100 in the mock sample were considered as appressorium stage induced genes as an early response, and the ones at 42 hpi were considered as biotrophic stage-specific. To identify protoplasting-induced genes, we performed RNA-seq using bulked samples. Arabidopsis leaves of 14-day-old seedlings were cut into 0.5 mm strips and digested in protoplast enzyme solution following the exact protocol used in single cell analysis. The protoplasts were collected and processed for total RNA isolation by RNeasy plant kit (Qiagen, [key resources table](#)) according to instructions provided by the manufacturer. Leaves directly collected from the seedlings without treatment were used as a mock control. Total RNA was quality checked by Bioanalyzer

and sent for sequencing. Raw reads of all the bulk RNA-seq data were fed for quality checking and adaptor removal by Trimmomatic.¹⁰² Trimmed reads were aligned against the Arabidopsis genome using Kallisto¹⁰⁴ followed by tximport¹¹⁴ to generate a count matrix. Batch effects removal was performed by the sva package.¹⁰⁶ Sample size factors, normalization, and differentially expressed genes were analyzed by DESeq2.¹⁰⁵ The protoplasting-induced genes were defined by a cut-off of $\log_2|FC| > 1$, $\text{padj} < 0.05$.

QUANTIFICATION AND STATISTICAL ANALYSIS

Statistical analyses were performed in R. One-way ANOVA Duncan test was used for multiple groups of observations. Student's t-test was used to determine the significance for two groups of observations. Details of the statistical analysis can be found in the figure legends.